Review

Radiobiological Applications of Vibrational Spectroscopy: A Review of Analyses of Ionising Radiation Effects in Biology and Medicine

Jade F. Monaghan [1,2], Hugh J. Byrne [3], Fiona M. Lyng [1,2] and Aidan D. Meade [1,2,*]

1   School of Physics, Clinical and Optometric Sciences, Technological University Dublin, Central Quad, City Campus, Grangegorman, D07 XT95 Dublin, Ireland; d16129286@mytudublin.ie (J.F.M.); fiona.lyng@tudublin.ie (F.M.L.)
2   Radiation and Environmental Science Centre, Physical to Life Sciences Research Hub, Technological University Dublin, Aungier Street, D02 HW71 Dublin, Ireland
3   Physical to Life Sciences Research Hub, Technological University Dublin, Aungier Street, D02 HW71 Dublin, Ireland; hugh.byrne@tudublin.ie
*   Correspondence: aidan.meade@tudublin.ie

Simple Summary: Radiotherapy is prevalent in cancer treatment, highlighting the critical need to understand the biological consequences of radiation exposure. This research aims to explore the contribution of vibrational spectroscopic techniques in understanding how radiation can affect molecular structures and biochemical processes within biological systems. These non-destructive methods can detect specific molecular vibrations, offering profound insights into, for example, DNA damage, lipid peroxidation, and protein and metabolic modifications induced by radiation. Identifying and understanding these changes, there is potential to improve radiotherapeutic outcomes, tailor treatments to individual patients, and enhance the understanding of radiation's biological effects, which could significantly benefit the research and clinical communities.

Abstract: Vibrational spectroscopic techniques, such as Fourier transform infrared (FTIR) absorption and Raman spectroscopy (RS), offer unique and detailed biochemical fingerprints by detecting specific molecular vibrations within samples. These techniques provide profound insights into the molecular alterations induced by ionising radiation, which are both complex and multifaceted. This paper reviews the application of rapid and label-free vibrational spectroscopic methods for assessing biological radiation responses. These assessments span from early compartmentalised models such as DNA, lipid membranes, and vesicles to comprehensive evaluations in various living biological models, including tissues, cells, and organisms of diverse origins. The review also discusses future perspectives, highlighting how the field is overcoming methodological limitations. RS and FTIR have demonstrated significant potential in detecting radiation-induced biomolecular alternations, which may facilitate the identification of radiation exposure spectral biomarkers/profiles.

Keywords: ionising radiation; Raman spectroscopy; FTIR spectroscopy; biological response

1. Introduction

Radiobiology is an interdisciplinary science that focuses on the biological effects of ionising radiation on biological material and living systems. It is a well-established discipline, the first observation of the biological effects of exposure to ionising radiation dating back to the late nineteenth century [1,2].

Over the years, researchers have employed various techniques to unravel complex cellular responses to ionising radiation, but none is considered suitable for clinical use due to conflicting results and numerous technical limitations, including but not limited to the use of stains and fluorescent tags, poor reproducibility, observer subjectivity, slow

turn-around time for results, and inter-laboratory variability [3–12]. However, vibrational spectroscopies, including Fourier transform infrared (FTIR) absorption and Raman spectroscopy (RS), are non-destructive, label-free bioanalytical techniques offering valuable insights into the molecular composition of tissue, cells, and biofluids. The global biomolecular information obtained from analysis with FTIR or RS renders them attractive modalities of analysis for the evaluation of the effects of radiation exposure (X-ray, γ-radiation, and particulate radiation) in a range of biological models (compartmentalised and living systems), including applications such as:

- Investigation of the biomolecular response to radiation.
- Evaluation of intrinsic radiosensitivity and radioresistance.
- Prediction of radiobiological and clinical therapeutic responses.

Many of the more recent studies in this review involve the investigation of the effects of irradiation at clinically relevant doses and modalities used in radiotherapy (such as external beam radiation therapy (EBRT), stereotactic ablative radiotherapy (SABR), and intensity-modulated radiation therapy (IMRT)), highlighting the alignment of the field with clinical advancements in radiotherapy.

Additionally, recent exploratory translational studies have shown promising results in utilising biomolecular information to discern individual responses to radiotherapy. Identifying radiosensitive and radioresistant responders before beginning radiotherapy would be clinically beneficial, as stratifying patients according to the risk of toxicity development would allow dose escalation in radioresistant patients and dose reduction or alternative therapeutic strategies in radiosensitive patients to minimise side effects and toxicities, which in some cases can be irreversible [13–16].

1.1. Vibrational Spectroscopy—Theoretical Aspects

Vibrational spectroscopic techniques like RS and FTIR offer several advantages over a range of research techniques used to assess radiation response, such as cell based assays, clonogenic assays, G2 assay, DNA-damage based assays, γ-H2AX foci assay, radiogenomics, and proteomics [17–21], as they are non-destructive, label-free, require minimal sample preparation, deliver rapid analysis, and are cost-effective methods for analysing cells, tissues, biofluids, xenografts, and bone samples. These optical techniques provide information about the detailed biochemical composition of a sample, often referred to as 'biochemical fingerprints', which represent intrinsic vibrational modes of molecules. As simply described by R.P. Feynman [22], "Everything that living things can do can be understood in terms of jigglings and wigglings of atoms."

The intensity and frequency (or wavelength; direct inverse relationship with frequency) of Raman and IR peaks reveal molecular composition (DNA, lipids, proteins etc.) and concentration within a biological sample. Coupled with microscopes [23–25], RS and FTIR are attractive choices for studying the molecular profile of biological materials in various biomedical applications, including radiobiology.

As optical spectroscopic techniques, they rely on the fundamental interactions between light and matter. When a sample is irradiated with electromagnetic radiation, such as light, interactions occur through reflectance, scattering, absorption, or transmission (Figure 1A), resulting in transitions between the vibrational states. Biological spectroscopic signatures consist of molecular vibrational modes, such as stretching (symmetric and asymmetrical) and bending (in-plane (scissoring and rocking) and out-of-plane (wagging and twisting)) (Figure 1B).
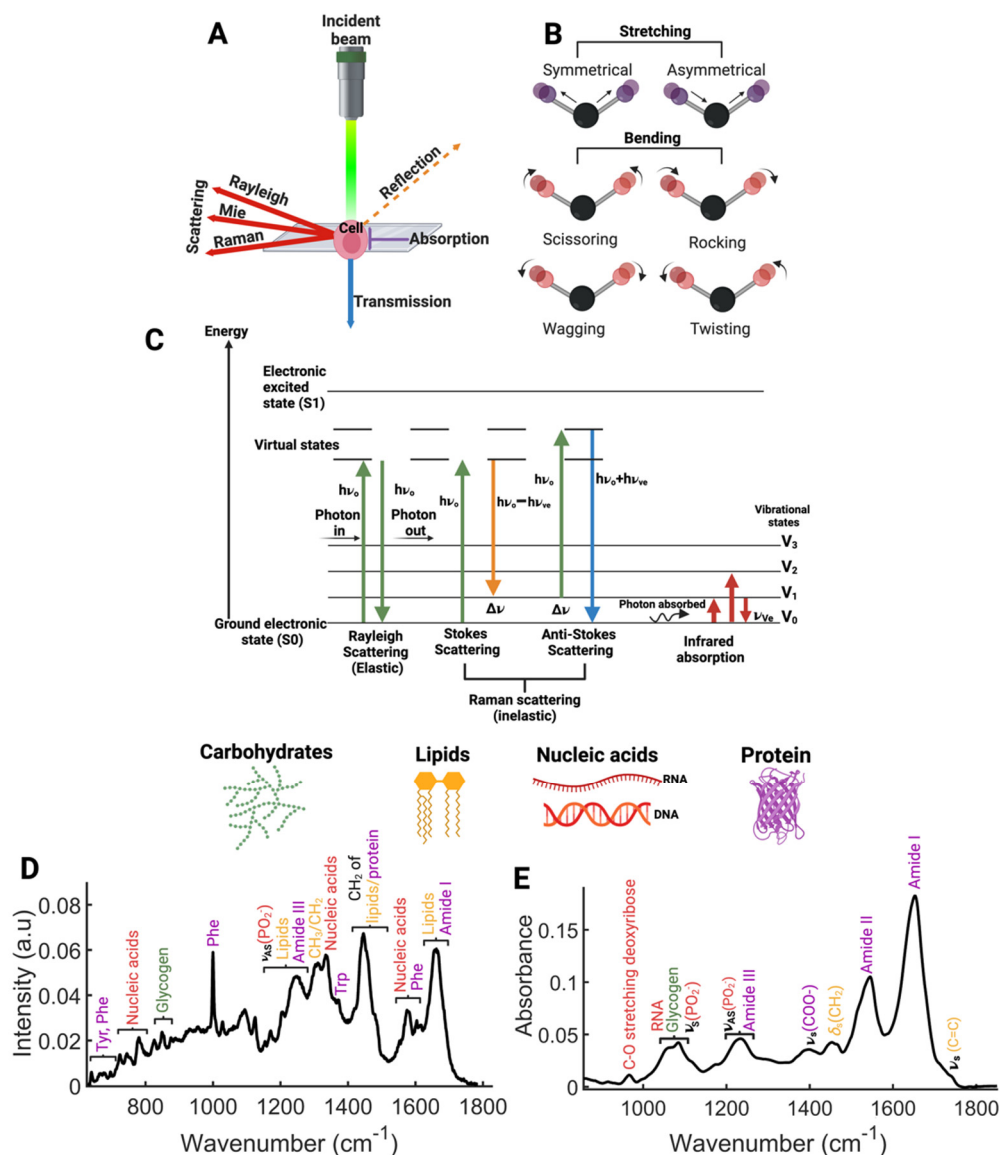
Figure 1. Basic principles of vibrational spectroscopy. (**A**) Interactions of incident light with a biological sample resulting in scattering (Mie, Raman (photons gain or lose energy), and Rayleigh (no change in photon energy)), reflection, absorption, and transmission of photons. (**B**) Graphical representation of stretching and bending vibrational modes of biomolecules due to interaction with the incident beam. (**C**) Energy-level diagram of IR (absorption, transmission and reflectance) and Raman scattering processes: $H\nu_0$ = incident laser energy, $h\nu_{ve}$ = vibrational energy, ν_{ve} = vibrational frequencies and $\Delta\nu$ = Raman shift (energy difference between the incident beam and scattered photons; expressed as wavenumbers). At room temperature, the majority of molecules are in the S0 state. Thus, a larger proportion of molecules will exhibit Stokes Raman scattering. Typical Raman (**D**) and FTIR (**E**) spectra of a cell, where ν = stretching vibrations, δ = bending vibrations, s = symmetric vibrations, as = asymmetric vibrations, phe = phenylalanine, tyr = tyrosine and trp = tryptophan.

Although there are fundamental differences between the spectroscopies, the Raman effect being a scattering process and IR spectra originating in an absorption process (Figure 1C), each spectroscopic modality provides detailed biochemical information, and mutually they act as highly complementary techniques, due to differences in the selection rules of their respective processes (changes in polarisability and dipole moment, respectively) [26].

By employing both spectroscopies for biological analysis, a more complete picture of the biomolecular fingerprint of the sample can be obtained. For instance, bonds that are centrosymmetric and display Raman activity will be inactive in IR, and conversely, those inactive in Raman will be active in IR [27].

The spectra of intensities within IR and RS spectra are commonly plotted against wavenumber (cm^{-1}). Wavenumbers (cm^{-1}) provide a direct correlation with energy levels of molecular vibrations and are inversely related to wavelength [28], making them particularly useful for expressing vibrational frequencies in a way that is directly comparable across different studies and instruments.

Biological materials are commonly analysed over the fingerprint region of Raman (400–1500 cm^{-1}) and IR (600–1500 cm^{-1}) spectra [29–31], and the major biological assignments across the spectral regions related to proteins, nucleic acids, carbohydrates, and lipids are highlighted in Figure 1D,E.

Spectral changes observed in the fingerprint region, whether induced by exogenous and endogenous factors or inherent sample characteristics, imply structural or biochemical changes within the sample. Variations in vibrational energy states due to bond formation, breakage, or changes in the molecular environment can shift the position and intensity of spectral peaks. The reader is referred to work by Movasaghi et al. [32,33] and Talari et al. [34] for interpretation of Raman and FTIR signatures and their tentatively assigned biological characteristics.

Both IR and RS spectra can be assessed qualitatively (position of spectral bands related to specific vibrational frequencies of individual molecules) and quantitively (the spectral band intensity is associated with molecular concentration) [26].

1.2. Raman and FTIR Instrumentation

Lasers serve as ideal probes in Raman spectroscopy due to their highly monochromatic characteristics and small beam diameters, enabling the analysis of areas as small as 1 μm^2 [35,36]. Commonly used laser wavelengths include 532 nm, 660 nm, and 785 nm and are introduced into the system via a pinhole aperture [37]. A clean-up filter ensures that only the precise laser wavelength is transmitted, and a filter wheel modulates the laser power [38]. The laser beam is then directed by a mirror towards a beam splitter, which primarily channels light through the objective lens to the sample, while some light can be diverted to a microscope camera for precise sample positioning and focusing [39]. Upon interaction with the sample, the laser is scattered, both inelastically (Raman) and elastically (Rayleigh) [40]. Raman scattering arises from the interaction of the laser light with vibrational modes of the molecular bonds in the sample, resulting in a shift in frequency that corresponds to the frequency of these molecular vibrations [41]. This scattered light re-enters the system via the objective lens and is redirected by the beam splitter to an edge/notch filter that selectively blocks the Rayleigh-scattered light, allowing only the Raman-scattered light to proceed [42]. The transmitted Raman scattering is then focused by a lens on an adjustable confocal pinhole aperture, which excludes out-of-focus light, thereby improving spatial resolution and enabling high-precision depth profiling [43]. The filtered Raman signal is dispersed by a diffraction grating into its constituent wavelengths and projected onto a charge-coupled device (CCD) array detector [44]. The CCD, a silicon-based multichannel array, converts light into electronic signals based on the number of photons detected [45]. These signals are then digitised and displayed as a Raman spectrum, which plots light intensity against wavenumber (cm^{-1}) [46]. A schematic of an experimental setup of a Raman spectrometer is provided in Figure 2A.

In an FTIR system (Figure 2B), a polychromatic infrared light source is directed into a Michelson interferometer [47], where the incident beam is first collimated into a parallel beam [48]. A beam splitter then divides this light, reflecting 50% toward a fixed mirror and transmitting the remaining 50% toward a moving mirror [49]. The reflected beams from both mirrors are recombined at the beam splitter, with the moving mirror inducing a varying optical path difference between the two beams [50,51]. When the optical

paths are equal, constructive interference occurs (in phase; maximum intensity), whereas unequal paths result in destructive interference (out of phase; minimal intensity) [52]. The resulting interference exits the interferometer and is directed by the lower dichroic mirror to the lower Cassegrain, then through the sample on an optical substrate, such as glass or calcium fluoride (CaF_2). As infrared light interacts with the sample, specific frequencies corresponding to the molecular vibrations of the samples chemical bonds are absorbed. The transmitted light is then directed to the mercury cadmium telluride (MCT) detector. The detector digitises the interference pattern in real time, producing an interferogram, a plot of signal intensity versus optical path difference created by the moving mirrors inside the interferometer [48,53]. Finally, a Fourier transform is applied to the interferogram, converting it into an IR spectrum as a function of wavenumber (cm^{-1}), which when ratioed with a reference is displayed as a transmittance, or absorbance spectrum [46]. The radiation protocols conducted before spectral acquisition vary across the studies reported. Detailed information can be found in the original sources.
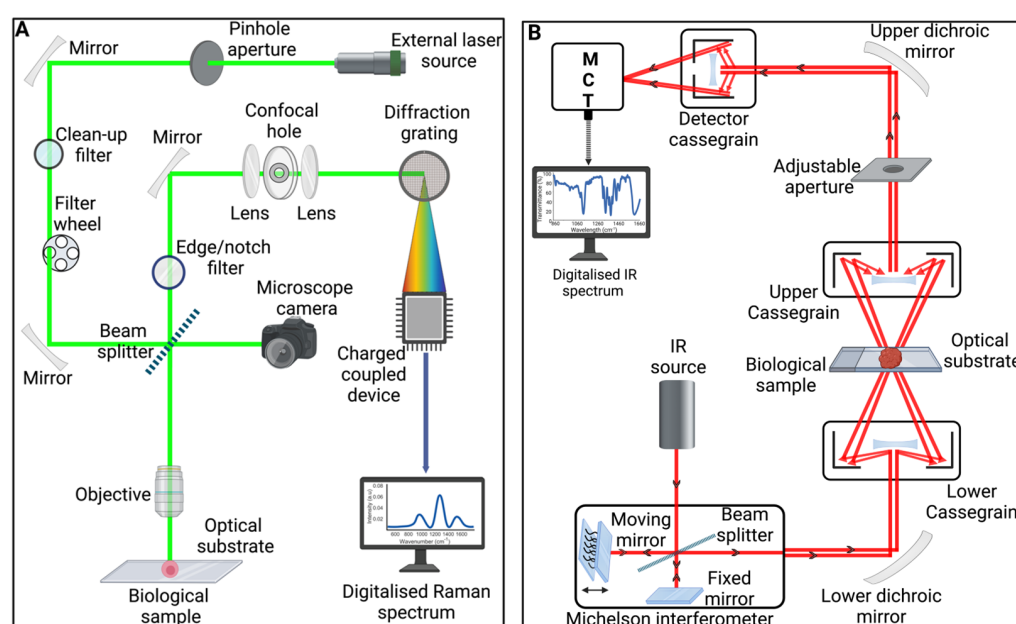

Figure 2. Schematic diagrams of the experimental set of a Raman (**A**) and FTIR (**B**) spectrometer.

1.3. Data Pre-Processing and Analysis Techniques

Pre-processing is the initial phase of the spectral data treatment pipeline and is conducted prior to multivariate analysis or machine learning. Given that Raman and FTIR spectroscopy are inherently sensitive techniques, it is possible for identical samples measured under the same test conditions to produce varying results, due to external influences (instrumental or environmental [54]. Additionally, a number of undesirable signals can arise from various sources, such as the state of the sample, fluctuations in source power, atmosphere, peak shifts, detector background noise, substrate signals, cosmic spikes, Gaussian noise (mainly from detector readout and dark current), scattering, and fluorescence [55–57]. If these are included in multivariate analysis, they could lead to misinterpretation of spectral outcomes. Therefore, harmonisation of spectral datasets through pre-processing methodologies is essential to ensure the removal of unwanted noise, artefacts, and variations while preserving the quality/integrity of the spectral data [58].

The choice of pre-processing method is not universal: it is highly dependent on the nature of the sample and the analysis modality. A typical pre-processing workflow used for cell and plasma Raman and FTIR spectra is outlined in Figure 3.
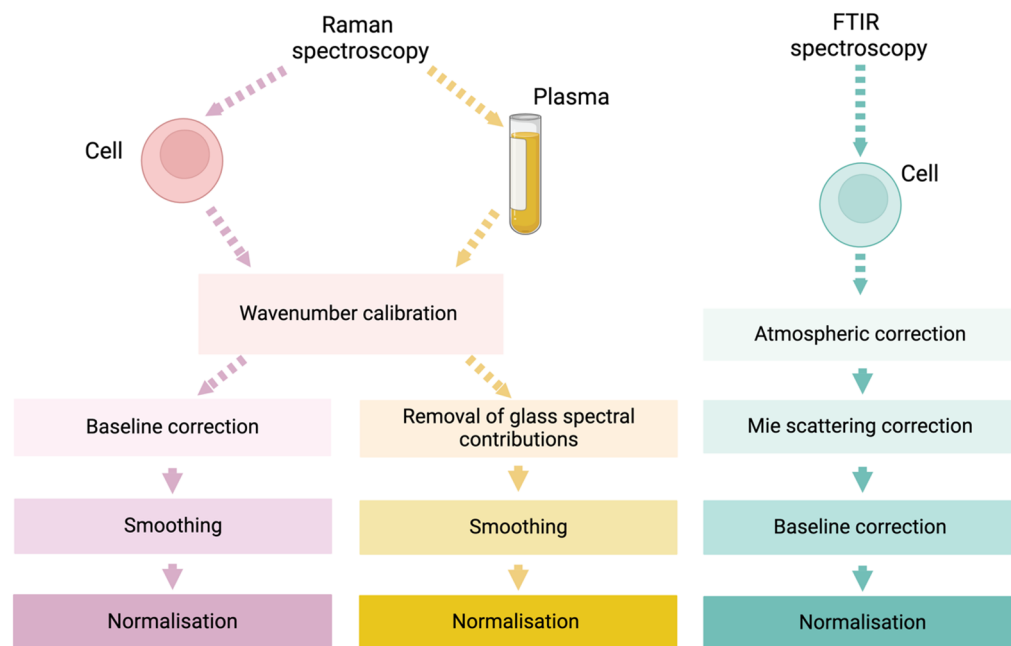
Figure 3. Example of a pre-processing workflow for cell and plasma Raman spectra and cell FTIR spectra.

Although not a true pre-processing step, initial calibration of a Raman spectroscopic detector must be performed using the 520.8 cm^{-1} band of crystalline silicon, whereby pixels in the CCD camera are assigned wavenumber values (*X*-axis) [59]. During spectral analysis, miscalibration of the system components can occur due to ambient room temperatures and/or misalignment of optical components [60], necessitating an additional *X*-axis alignment procedure on raw Raman spectra using a reference compound, for example, benzene, indene, and 4-acetamidophenol, which display defined Raman bands across a broad wavenumber range [61]. Strong interference from optical substrates, such as glass, can be removed using the extended multiplicative signal correction (EMSC) algorithm [62]. Smoothing techniques, such as the polynomial-based Savitzky–Golay filter, can be applied to remove unwanted noise while preserving the shapes of spectral peaks [58,63]. Baseline distortions in both Raman and FTIR spectroscopy arising from sample or instrument changes can be corrected by using numerous methods such as median window, differentiation, polynomial fitting, and asymmetric least squares-based methods [58]. Before any further analysis, combination, or comparison, the intensity ranges of spectra should be standardised using a normalisation procedure [64].

In FTIR analysis, a common challenge is the interference of H_2O and CO_2 absorption bands [65]. This interference can be addressed by subtracting a scaled atmospheric reference spectrum for regions affected by these environmental conditions [66]. The size of human cells (~8–30 μm) and cellular machinery (1–10 μm) is comparable to mid-infrared radiation wavelengths (3–10 μm), resulting in spectral distortion due to intense scattering, known as resonant Mie scattering (RMieS) [55,67]. This distortion can be corrected using the RMieS-ESMC algorithm [55].

Multivariate statistical analysis is commonplace in Raman and FTIR studies, as it is capable of handling multiple independent variables simultaneously [68]. Principal component analysis (PCA) is an unsupervised dimensionality reduction technique used extensively for exploratory data visualisation, facilitating the identification of clusters, patterns, and outliers in spectroscopic datasets. In brief, PCA uses orthogonal transformations to generate a set of linearly uncorrelated variables known as principal components (PCs) [69]. The first principal component (PC), PC1, represents the direction of greatest variance in the data, carrying the pattern with the largest portion of information [58]. PC2 captures the largest orthogonal residual variance relative to PC1, with subsequent PCs

capturing additional variations. The goal of PCA is to reduce the dimensionality of a high-dimensional dataset while retaining as much information as possible [70].

Following exploratory data analysis, machine learning classifiers are typically applied for data prediction or classification. This can be performed on PCA-transformed or pre-processed data, the former approach allowing for modelling based on the insights gained during PCA.

A commonly used technique for analysing high-dimensional datasets in which the number of features exceeds the number of observations, such as Raman and FTIR spectral data [71–73], is PLS-DA [74–79]. It functions as a two-class linear classifier, identifying a hyperplane in the multi-dimensional feature space that separates class labels (Y) based on spectral data (X). It maximises the covariance between X and Y and linearly transforms the data into a lower-dimensional subspace defined by latent variables (LVs) for improved prediction and analysis [80]. Unlike partial least squares regression (PLS-R), which models the association between spectral data and numerically continuous targets like dose (Gy) [81–84], PLS-DA combines PLS-R with linear discriminant analysis (LDA) [85] and uses categorical labels for classification, such as different late-toxicity grades developed by patients following radiotherapy [75,76]. Other classification algorithms used in the field include PCA-LDA [78,86–88], PCA–quadratic discriminant analysis (QDA) [78], PCA–random forest (RF) [89], support vector machine (SVM) [82,90], and K-nearest neighbour (KNN) [78].

This review depicts the arc of the evolution of this subfield of radiation biology and radiation science, tracing its historical roots and charting its progress towards translational applications. It also offers a perspective on the future application of these techniques and other advancements in relation to providing insights into the biological response induced by ionising radiation.

2. Historical Developments

2.1. Studies of Model Systems

In the early exploration of vibrational spectroscopy in radiation science, Marcus and Corelli [91] investigated the effects of ionising radiation on purines and pyrimidines and their derivatives using FTIR spectroscopy. Changes in bands at 1205, 1415, 1445, and 1660 cm^{-1} and increasing absorbance at 2900 cm^{-1} were found for adenine, thymine, guanine, and cytosine following high radiation doses, whereas uracil did not show spectral changes. Bases containing side groups, such as methyl and ethyl groups, were found to be more susceptible to radiation damage.

Building on this pioneering work, Verma et al. performed studies of model membranes with RS using 514.5 nm as source after irradiation with γ-ray doses up to 30 Gy [92–94]. They observed radiation-induced decreases in phospholipid unsaturation and increases in their *trans* configurations in dipalmitoyl lecithin and polyunsaturated liposomes (their interpretation was based on ratios of the *trans* vibration of C–C at 1064 cm^{-1} and its *gauche* vibration at 1090 cm^{-1}, together with ratios of the *cis* C=C stretching vibration at 1660 cm^{-1} and C–H deformation vibration at 1440 cm^{-1}). They also observed the amelioration of this effect by the incorporation of proteins within these model membrane systems. In these and further studies [95], changes in the secondary structure of proteins within the model system were inferred by changes in spectral regions assigned to the amide I, amide III, and side-chain amino acid groups, with modifications to features in the region from 550 cm^{-1} to 1030 cm^{-1}, suggesting that the tyrosine and cysteine side groups are particularly radiosensitive. Sailer et al. [96] also studied peroxidation and cytochrome-C-induced damage in model membrane systems with FTIR after γ-ray doses of 100 Gy.

FTIR spectroscopy was used by Kinder et al. [97] to study lipid peroxidation induced by γ-ray radiation in liposomes of dilinoleoyl-glycero-3-phosphocholine. The main spectral changes observed were a decrease in the 3010 cm^{-1} band, assigned to the asymmetric C–H stretching vibration, a shift in the asymmetric phosphate ester stretching vibration from 1260 to 1244 cm^{-1}, and a new band at 1693 cm^{-1} associated with the formation of unsaturated aldehydes 48–72 h after irradiation with doses greater than 100 Gy.

Further studies by Torreggiani et al. on lysozyme radical degradation in a protein–liposome model after doses of 33 Gy to 1 kGy suggested an increase in disordered protein structures based on a shift in the amide I vibration (from 1660 to 1667 cm^{-1}) and increased hydrophobicity of the tryptophan and tyrosine side chains of the molecule after irradiation (using, for tryptophan, the shift of the band at 877 cm^{-1} to 880 cm^{-1}, and the ratio of intensities of the tyrosine 850 cm^{-1} to 830 cm^{-1} doublet) [98].

Sailer et al. also studied γ-irradiation-induced damage (with doses from 0 to 40 kGy) in double-stranded DNA [99] with FT-RS, whereby they observed spectral changes which were interpreted as strand breaks, base damage, base-unstacking and pre-melting effects, and disordering of the deoxyribose backbone in B-DNA. Synytsya et al. confirmed these findings in double-stranded DNA with RS using a source wavelength of 632.8 nm [100], and also analysed the effects of proton and γ-irradiation on bovine and human serum albumin [101]. They observed spectral changes that they interpreted as increases in the β-sheet structure and disordered structures of these proteins after irradiation, together with a decrease in the intensity of bands associated with phenylalanine, tyrosine, and tryptophan (and shifts in the vibration mode of tryptophan of 4–6 cm^{-1}). Further indications of the effect on the conformation of the protein structures were the observation of a dose-dependent decrease in the C–S vibration in cysteine and methionine and a similar decrease in C–C and C–N vibrations of aliphatic amino acids (such as aspartine and glutamine). Similarly, proton irradiation of bovine serum albumin (BSA) resulted in changes in the profile of the amide I band, indicative of changes in protein secondary structure, involving a decrease in the α-helical component and an increase in the β-sheet component [102].

FTIR spectroscopy was also used to study DNA isolated from epididymis cells of rats exposed to low-dose irradiation in the Chernobyl exclusion zone [103]. The main changes involved increases in the intensity of CH bands at 2850, 2886, 2918, and 2953 cm^{-1} and changes in C=O vibrations of thymine, guanine, and cytosine near 1710, 1700, and 1656 cm^{-1}. Online RS was used to monitor X-ray damage in brominated DNA crystals [104]. X-ray-induced debromination was monitored in real time at increasing doses to 5 MGy by following the decay of the non-symmetric bending vibration for the C–Br bond at 293 cm^{-1}.

Torregiani et al. also performed studies with RS and HPLC on γ-irradiated RNase A in aqueous solutions and lipid vesicles [105], observing spectral changes consistent with exposure of tyrosine residues and breakages in the S–S and C–S bonds in the molecule after adjustments to its conformation. This result was confirmed by parallel observation of variations of the α-helix and β-sheet content of the molecule in the amide I and amide III bands.

Ultraviolet resonance (UV)-RS, as utilised by Shaw et al. [106], facilitated an investigation into the effects of cobalt-60 γ-irradiation (2000 Gy) on calf-thymus DNA (CT-DNA) and a short-stranded DNA oligomer (SS-DNA). This investigation indicated that both types of DNA experienced unstacking of their bases, the effect being notably more significant in CT-DNA. This was deduced from the observed increase in the intensity of Raman bands associated with ring modes and vibrations characteristic of adenine, cytosine, guanine, and thymine (1240, 1252, 1375, 1421, 1486, 1576, 1604, 1650, 1673, and 1690 cm^{-1}). Additionally, changes in the hydrogen bonds within base pairs were observed, manifested as a downshift in the wavenumber position of the 1604 cm^{-1} band, highlighting the profound impact of such radiation on DNA structural integrity. For SS-DNA, the results pointed to a considerable disruption in nucleotide structure, evidenced by a reduction in the intensity of DNA-associated Raman signatures.

It is worthy of note that most of the investigations involving compartmentalised models were carried out at relatively high radiation doses.

2.2. Studies of Microorganisms

In the first applications of FTIR spectroscopy to the analysis of radiation-induced damage in cellular organisms, Melin.et al. used spectral data to examine γ-irradiation damage (after doses from 0 Gy to 24 kGy) in *Deinococcus radiodurans* [107], *Kocuria rosea* [108] and *Micrococcus luteus* [108]. *Deinococcus radiodurans* is a red aerobic bacterium (containing

high carotenoid levels) found in meat. Samples of the bacterium were cultured on zinc-selenide (ZnSe) discs, dried, and their spectra were recorded at a resolution of 6 cm^{-1} from 4000 cm^{-1} to 500 cm^{-1}. Hierarchical cluster analysis (HCA) employing first-derivative spectra and Ward's clustering algorithm was used to identify a threshold of 10 kGy for the initiation of spectral change representative of DNA damage (asymmetric and symmetric stretching vibrations in the phosphodiester backbone) in the 1200–900 cm^{-1} range. The significance of spectral changes in difference spectra was examined using Student's *t*-test. This identified an increase in fatty acid spectral features (CH$_2$ antisymmetric and symmetric stretches at 2932 cm^{-1} and 2854 cm^{-1}, respectively), a decrease in carbonyl stretch in lipid and nucleic acid (at 1742 cm^{-1} and 1712 cm^{-1} respectively), and a decrease in amide I, amide II, and COO$^-$ stretching vibrations in protein and amino acids (with a slight spectral shift in the amide I band). They interpreted these spectral changes as signifying an increased length or enhanced synthesis of lipid, glycophospholipid, and increased protein denaturation and proteolysis. Increases in phosphate stretching vibrations (asymmetric at 1245 cm^{-1} and symmetric at 1085 cm^{-1}) and decreases in deoxyribosyl, ribosyl, and glucosyl vibrations were also observed (at 1145 cm^{-1}, 1040/992 cm^{-1}, and 1030 cm^{-1}, respectively). These persisted after reincubation of the bacterial cells, and were interpreted as signifying alterations to carbohydrate structures (strand breaks, oxidisation of bases in nucleic acids as a result of free radical attack). In studies by Melin et al. [108] and Perromat et al. [109] on *M. Luteus* (yellow-pigmented bacterium) and *K. Rosea* (red-pigmented bacterium) using the same analytical approaches (and with γ-irradiation doses from 0 Gy to 16.4 kGy (*M. Luteus*) and 22 kGy (*K. rosea*)), modifications to polysaccharide bond vibrations in the fingerprint region and evidence of strand breakage and decreases in DNA content were observed.

DNA extracted from the radioresistant bacterium *Pantoea agglomerans* was irradiated at doses up to 16 kGy, and FTIR spectra showed intensity increases in bands assigned to carbonyl (1692 cm^{-1}), NH$_2$ scissoring (1605 cm^{-1}), and N-H bending vibration (1560 cm^{-1}) [110]. At doses greater than 5 kGy, there was also a shift in the symmetric PO$_2$ band from 1070 to 1088 cm^{-1} and a new band at 1164 cm^{-1} as a result of the phosphodiester bonds and/or the opening of ring deoxyribose.

3. Studies on Subcellular, Cellular, Tissue, and Bone Systems In Vitro and Ex Vivo

3.1. Direct Irradiation Studies of Subcellular Systems

The lens of the eye is considered to be one of the most radiosensitive tissues, and human lens opacification occurs at low doses (<0.1 Gy) [111]. At a low dose of 0.25 Gy X-ray irradiation, glutamate (808 cm^{-1} and 1056 cm^{-1}), a marker of oxidative damage, was found to be more abundant in human lens epithelial cells (both cytoplasm and nucleus) compared to control cells using RS [112].

In one of the first studies in this domain, Lasalvia et al. [113] compared the spectral features of the nucleolus with the nucleoplasm of human breast epithelial cells (MCF10A) 24 h following proton irradiation at a range of doses (0.5, 2, and 4 Gy). Even at the lowest dose, a reduction in the intensity of bands centred at 784 cm^{-1} (O–P–O stretching mode of the phosphodiester bond of the phosphate group) and 1096 cm^{-1} (PO$_2$$^-$ phosphodioxy bond of the phosphate group) was observed [113]. These findings corroborate the group's previous findings of whole-cell analysis of MCF10A cells, which demonstrates the sensitivity of phosphate groups to proton irradiation [114].

Using synchrotron radiation (SR)–FTIR for the analysis of single nuclei of glioblastoma cells following proton irradiation at 1 and 10 Gy, Lipiec and colleagues observed a decrease in the intensity of the nucleic acid base stacking mode (C=O stetching mode; 1713 cm^{-1}) [115], suggestive of base-pair damage. They further observed that irradiation at 10 Gy significantly alters lipid accumulation, biosynthesis, and membrane fluidity via spectroscopic alterations at 1418 cm^{-1}, 1468 cm^{-1} and 2750–3100 cm^{-1}, and further spectroscopic markers were observed via atomic force microscopy IR (AFM-IR) spectra at 1464 and 2920 cm^{-1}, most of these spectroscopic biomarkers representing cholesterol and its esters.

To interrogate the differential dose-dependent effects of radiation on the cytoplasm and nucleus, Delfino et al. [116] utilised the Raman difference spectra of nuclear and cytoplasmic spectra measured in neuroblastoma cells (SH-SY5Y) fixed immediately post-X-ray irradiation (2–8 Gy). They observed an increase in the intensity of the signatures of nucleobases (677, 722, 1344, and 1374 cm^{-1}), parallel and anti-parallel β-sheet secondary structures (1640 cm^{-1}), and protein/lipid CH_3 asymmetric stretching (2955 cm^{-1}) with dose, and conversely, decreasing intensities of the DNA and/or RNA backbone (780, 807, 1325, and 1430 cm^{-1}), α-helix secondary structure (1661 cm^{-1}), and the CH_2 symmetric and asymmetric and stretching of carbohydrates and lipids (2860 and 2940 cm^{-1}). In further corroborating work by Delfino et al. [117], Raman spectral features of the nucleus were found to be altered to a greater extent than those of the cytoplasm. At a dose of 2 Gy, spectral changes consisted of changes in intensity ratios of Raman spectral signatures related to lipid saturation, suggesting nuclear softening [118].

In a pilot study by Roman et al. [81], Raman mapping of whole prostate cancer cells (PC-3) 24 h following high-dose X-ray irradiation (10, 30, and 50 Gy) also revealed distinct differences in spectral patterns of lipids and DNA between the nucleus and cytoplasmic regions. Follow-up studies by Roman and colleagues [83,84] incorporated PLSR to quantify X-ray doses delivered to the previously investigated subcellular compartments, revealing spectral trends indicative of DNA damage and lipid changes dependent on fixation time (cells fixed immediately and 24 h post irradiation (early-stage biological response) and cells fixed before irradiation (physicochemical response)) and irradiation dose (low–clinical and high doses). Cytoplasmic lipid concentration of PC-3 cells, rather than lipid composition, was also found to be significantly altered by X-ray irradiation (10, 30, and 50 Gy), i.e., metabolic pathways of lipid metabolism are targeted, affecting lipid homeostasis [119]. Therefore, examining different subcellular components separately is crucial for a complete and accurate interpretation of the cellular responses to radiation exposure.

3.2. Direct Irradiation Studies of Cells

FTIR spectroscopy has shown potential to detect radiation-induced apoptosis-related signals in a colorectal carcinoma cell model after low-dose α-particle irradiation (0.5–3 Gy) [120] and in γ-irradiated lymphocytes (6 Gy) [121]. Here, significant spectral shifts and intensity alternations that indicated increased DNA hydrogen bonding and conformational changes (1242 cm^{-1} to 1234 cm^{-1} and 1090 cm^{-1} to 1086 cm^{-1}; phosphate bond vibrations), changes in protein synthesis or degradation (increases in amide I: 1650 cm^{-1} and amide II: 1540 cm^{-1} bands), and alterations in lipid structures (1733 cm^{-1} and 1742 cm^{-1}) were observed [121].

Human keratinocyte (HaCaT) cells exposed to a similar dose of γ-irradiation [122] and α-particle exposure [123] exhibit similar types of molecular damage as previously reported [121], the latter resulting in greater absorbance differences, indicating a greater amount of unrepaired radiation damage [123].

Chemometric analysis indicates that the extent of damage induced by γ-irradiation to HaCaT cells varies, depending on dose (0, 0.05 and 5 Gy) and post-irradiation time (6–96 h) [124]. A reduction in the changes to biochemical content was observed with respect to dose and time, likely due to the cessation of radiation-induced cellular response mechanisms. Modifications were mostly related to DNA, RNA (996, 1084, 1090 and 1230 cm^{-1})- and carbohydrate (1030–1290 cm^{-1})-related FTIR signatures. These findings point to the potential of FTIR spectroscopy for applications in retrospective biodosimetry.

Furthermore, γ-irradiation at clinically relevant doses induces distinct and temporally specific biochemical changes in breast (MCF7 and SKBR3) and gingivobuccal squamous cell carcinoma cells (ITOC-03) [125,126]. Initially, there are rapid modifications of RS bands associated with cytochromes (750 cm^{-1}) within 30 min [126], likely due to radiation-induced production of reactive oxygen species (ROS) [127]. Over a longer period (24 to 48 h), there is a marked decrease in lipid-associated RS signatures (2700–2800 cm^{-1}), reflecting a lasting alteration of lipid metabolism [125].

Nasopharyngeal cancer (NPC) is highly radiosensitive [128], and also has a high prevalence rate in Epstein–Barr virus (EBV) infection in endemic areas (China and Southeast Asia) [129,130]. Therefore, the effect of X-ray irradiation (2.3 Gy) on EBV-associated NPC (EBV+) and non-associated NPC (EBV-) cell lines was carried out by Qiu et al. [131] using laser tweezers LTs-RS. The study found that CNE2 cells (EBV-) were more susceptible to irradiation compared to C666-1 cells (EBV+; Figure 4A,B). Raman bands at 752 and 1335 cm^{-1} (ribose bands of purines and tyrosine) are associated with base unstacking resulting from radiation-induced DNA damage [131].
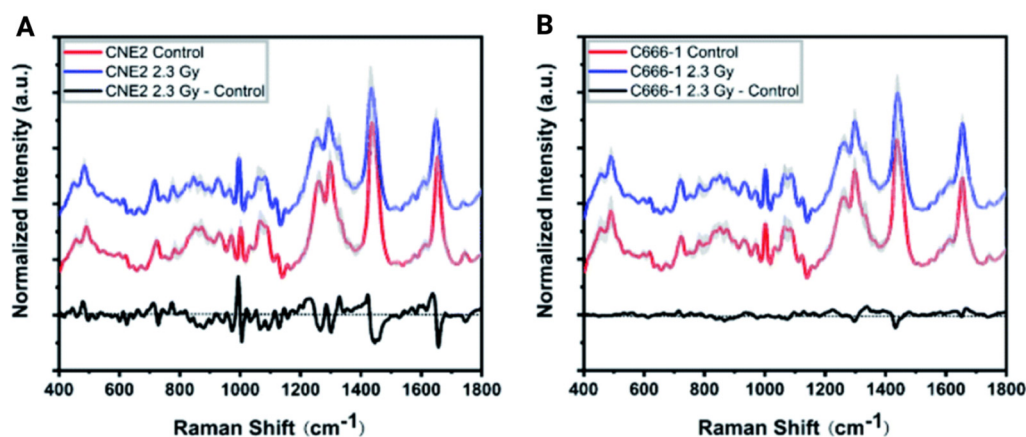

Figure 4. Effect of X-ray irradiation (2.3 Gy) on EBV+ and EBV- NPC cells. Comparison of mean LTs-RS spectra from (**A**) control group and radiated groups of CNE2 cells, (**B**) control group and radiated group of C666-1 cells [131]. The shaded areas (grey) indicate the standard deviations of means. The difference spectrum (2.3 Gy minus control) is shown at the bottom (black lines). Post-irradiation, radiosensitive CNE2 cells exhibited statistically significant DNA alterations, evidenced by changes in nucleic acid-related spectral bands (752, 1264, 1335 cm^{-1}), amide I and II (1264 cm^{-1} and 1655 cm^{-1}), and lipid bands (1065, 1297, and 1655 cm^{-1}).

In related work on the same cell type, similar SERS (surface-enhanced RS) signals associated with base unstacking were also noted [132].

Hill et al. [133] and Rauniyar et al. [134] both investigated Raman spectral variations in relation to the cell cycle phase and the effects of irradiation. Hill et al. [133] monitored these variations in brain tumour cells (UVW), either synchronised to the G1–S boundary prior to irradiation or left unsynchronised, 24 h after a 6 Gy dose of X-ray radiation. Notably, cells exhibit radioresistance toward the end of the G1 phase and into the S phase [135].

PCA revealed PC5 to be the most important for classifying the irradiated synchronised and unsynchronised cells (Figure 5A,B). The PC5 loading box plot in Figure 5A displays a significant increase in PC score between the control and the unsynchronised cells, indicating greater radiation-induced biochemical differences. Protein and amide III (963, 1235, 1429 and 1631 cm^{-1}) modifications were the most prominent biomolecular signals (Figure 5B) and could be attributed to activation of cell cycle repair processes.

Multiple studies collectively highlight that X-ray irradiation at incremental clinically relevant dose levels induces dose-dependent biochemical changes in various cell types (SH-SY5Y, HeLa, and M/10 (non-tumourigenic human mammary epithelial cell line), as evidenced by FTIR [136] and RS [137–140]. Spectral differences are initially evident following irradiation and include lipid accumulation suggestive of apoptosis (CH_2/CH_3 ratio 2923/2955 cm^{-1}) and differences in secondary protein rearrangement ratios, for example, amide I/amide II-α; 1652/1553 cm^{-1} [136]. However, within 24 h, a decrease in O=P=O stretching (1090/1405 cm^{-1}) was noted with increasing dose, indicative of DNA structure stiffening [138]. Other biochemical effects tend to diminish or shift towards repair processes due to the absence of dose-dependent spectral intervals 24 h post-irradiation [140].
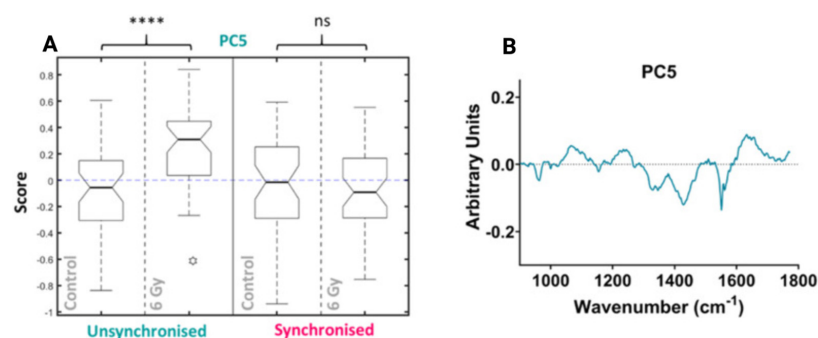
Figure 5. PCA of UVW Raman spectra 24 h post-irradiation. (**A**) Box plots of PC5 scores and irradiation dose and (**B**) PC loadings for PC5. Box plot compares control cells and 6 Gy irradiated cells for unsynchronised UVW cells and synchronised UVW cells [133]. Statistical analysis was performed using a two-way ANOVA with Wilcoxon rank sum test at 99% confidence interval ($p > 0.05$ = ns (not significant) band, $p < 0.0001$ = ****). Data points are represented as ○.

SR-FTIR spectra of prostate cancer cell models irradiated with protons (50, 200, 400, 2000, and 4000 Gy) exhibited spectral modifications related to lipid accumulation [141,142] similar to those induced by high doses of X-ray irradiation up to 30 Gy [143,144] and low-dose X-ray [136] and cone beam computed tomography radiation (33.59 mGy) [145]. Radiation-induced lipid modifications also include increases in ester-related bands (1740 and 1734 cm^{-1}) [142,145]. Additionally, a dose-dependent shift and intensity variations in FTIR bands associated with the O–P–O stretching mode of the phosphodiester bond in the DNA backbone was observed following proton exposure [141,142].

Matthews et al. [146] performed a study of photon (6 MV)-irradiated and non-irradiated prostate tumour cells with an innovative RS technique of live, single-cell analysis. This approach was used in subsequent work and allowed for the separation of Raman spectra based on cellular response to high-dose photon irradiation (0, 15, 30, 50 Gy) in radiosensitive prostate cancer cells (DU145/LNCaP) and radioresistant breast (MDA-MB-231)/prostate (PC3) and non-squamous cell lung cancer (NSCLC; H460) cancer cells/breast cancer cells (MCF7) [147].

RS of radioresistant H460 and MCF7 single cells showed similar statistically significant increases in glycogen-associated Raman bands (481, 579 and 710 cm^{-1}) after a 2 Gy dose of photon irradiation that extended to higher doses [148]. A radiogenic trend in glycogen levels in H460 and MCF7 cells was corroborated by subsequent investigations, the effect being more prominent in the former (Figure 6(Ai)), which showed a dependence on dose and time post-irradiation, and was spectroscopically observable as early as 24 h post-irradiation (Figure 6(Aii)) [149].

Similar trends in glycogen signatures for the radioresistant cell types were further confirmed in other work [74,150–154] and medulloblastoma cells (HTB-186 Daoy) [77]. However, a membrane lipid response to irradiation was noted in radiosensitive LNCaP cells [148,150,152]. In particular, phosphatidylcholine was seen to be one of the most distinguishing biomolecules between the radiosensitive and radioresistant cancer cell types [150].

When comparing lung and head-and-neck models based on radiation response, significant modifications in lipid/collagen and nucleobase-adenine (1340 cm^{-1}) RS-related bands were also highlighted following X-ray irradiation (8 Gy cumulative dose) [90] and γ-irradiation (50 Gy or 70 Gy cumulative dose) [155], respectively.

Such studies further demonstrate that intrinsic radiosensitivity plays a significant role in the response to radiation [156–160].

3.3. Direct Irradiation Studies on Tissues and Animal Model Studies

X-ray-irradiated freeze-dried sections of rat small intestines (low dose: 10 cGy), as well as γ-irradiated rat liver and brain tissues (800 cGy) and rat brain homogenate (1000 cGy), were

examined using FTIR [161–164]. In all doses explored in these studies, spectral signatures suggestive of lipid peroxidation were observed, such as an increase in olefinic =CH and CH_3 groups and carbonyl and a decrease in the lipid-to-protein ratio (CH_2 antisymmetric stretching + CH_2 symmetric stretching/amide I) and CH_2/lipid ratios [161,162]. Furthermore, HCA of rat brain homogenate spectra showed that proteins in the membranes, particularly amide I (1700–1600 cm^{-1}) and associated assignments, such as α-helix, β-sheet, and random coils, are more susceptible to radiation-induced damage than lipids [163].

A study by Harder et al. [165], explored the effects of photon irradiation on NSCLC xenografts in mice implanted with H460 cells, utilising RS. The findings revealed a significant change in the intensity of bands attributable to glycogen (482, 850, 940, 1042, 1083, 1129, and 1385 cm^{-1}) relative to the amide III and amide I bands (1661, 1447, 1240–1297 cm^{-1}) in response to irradiation doses of 5 or 15 Gy compared to non-irradiated tumours. This study underscores the value of RS in detecting in vivo radiation-induced responses even in the presence of a biochemically complex tumour tissue microenvironment [165]. Similar to the response of in vitro-irradiated H460 cells, glycogen accumulation was detectable in NSCLC xenograft Raman spectra from day 1 to day 10 post-in vivo X-ray irradiation at 15 Gy (Figure 6(Bi,Bii)) [166] and associated with tissue oxygenation [153,166]. Furthermore, the heterogeneity of glycogen accumulation, as evidenced by Raman mapping, is not only dose dependent but also heterogeneously distributed throughout the tumour [167].

Moreover, RS can effectively detect radiation response in MDA-MB-231 breast cancer xenografts [168] and be utilised as a predictive tool for evaluating the severity of radiation-induced lung fibrosis [169].
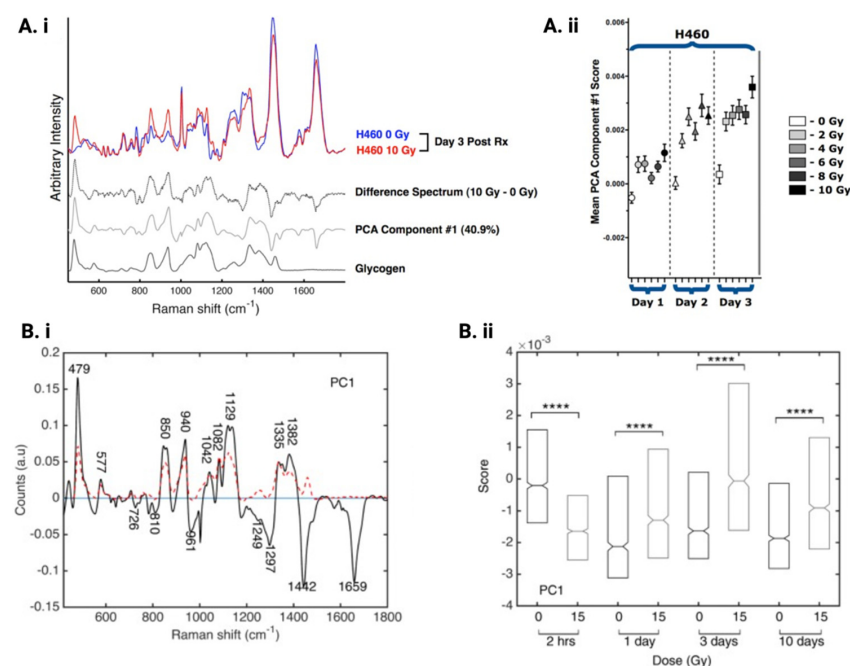

Figure 6. RS of H460 NSCLC cells and xenograft models detects radiation-induced glycogen accumulation. (**Ai**) Raman spectra of an irradiated (10 Gy) and unirradiated H460 cell (0 Gy) at 3 days post-irradiation demonstrating Raman spectroscopic detection of increased intracellular glycogen. The Raman spectrum of glycogen is shown for comparison with the difference spectrum and PC1 loading plot. (**Aii**) The mean PCA scores of H460 cell spectra for the first PCA component indicate statistically significant ($p < 0.05$ by unpaired two-tailed t-test) increases in intracellular glycogen over time relative to same day unirradiated cells [149]. (**Bi**) The black line represents PC 1 from PCA of H460 xenograft spectra in a single dose group (0 and 15 Gy) and time point (2 h and 1, 3, and 10 days post-irradiation). The dashed red trace represents the Raman spectrum of pure glycogen and (**Bii**) corresponding box plots of median PC1 scores [166]. Statistical analysis was performed using a two-sided Wilcoxon rank sum test to a 5% significance level. Statistical significance: **** $p \leq 0.0001$.

3.4. Non-Targeted Effects of Radiation (Bystander/Abscopal Effects)

Several studies have investigated non-targeted effects of radiation, such as bystander and abscopal effects, whereby effects are seen in cells or tissues that are not directly irradiated.

Key studies have demonstrated that low-dose in vitro non-targeted γ-irradiation (0.5 Gy) [170], and proton irradiation (1 or 2 MeV) [171] inhibit apoptotic signalling pathways in HaCaT cells, such as the mitogen-activated protein kinase (MAPK) pathway, which can be correlated with radiation-induced bystander exposure (RIBE) RS spectral signatures [170] and induce changes in SR-FTIR spectra of PC-3 cells, characterised by alterations in the DNA phosphate backbone, nucleobases, and protein secondary structure [171]. Recently, distinct biochemical alterations were observed in FTIR spectra of an in vitro prostate cancer model induced by different radiation exposure modes, including clinically relevant X-ray doses (2 Gy), low-dose scatter irradiation (0.2 Gy), and RIBE [172], providing a valuable means of assessing the effects of radiotherapeutic treatment on normal and cancerous tissues. Furthermore, consistent ATR (attenuated total reflectance)–FTIR spectral features in direct and indirect irradiation scenarios of rat tissues further underscore the pervasive nature of RIBE [173], which has also been reported to change the pH of cell culture media exposed to irradiated cells (2 Gy and 4 Gy) [174].

3.5. Direct Irradiation Studies of Bone Systems

Despite extensive research in radiation biology using RS and FTIR analysis for cells, tissues, and xenograft models, investigations focused on bone remain limited.

RS and various modalities of FTIR have consistently demonstrated that X-ray and γ-irradiation cause significant changes in mineral components (inorganic) and collagen matrix (organic) in murine and human bone tissue [175–180]. Persistent damage to bone tissue can also be detected using RS up to 26 weeks after irradiation [177]. Furthermore, pretreatment with amifostine has been shown to offer radioprotection to bone tissue [178,179] and animal tissue [162,163] by minimising radiation-induced spectral modifications.

In bovine bone, ATR–FTIR spectral modifications resulting from the delivery of high doses of radiation, commonly used for sterilisation of connective tissue allografts and preservation in bone banking, have also been mitigated by pretreatment with radical scavengers, hydroxytyrosol, and alpha-lipoic acid before γ-irradiation at a dose of 35 kGy [181]. Increasing X-ray and γ-irradiation doses up to 1000 kGy induces damage to human and bovine bone tissues [182–184]. This damage is observable in deep-UV and near-infrared (NIR) RS spectra as an increase with dose in intensity of the amide I band (1650 cm^{-1}), indicating changes in the protein secondary structure [183,184]. The potential of FTIR for bone-based dosimetry in health management following radiation exposure was also previously showcased [185], with similar investigations extending to human hair and whole blood [79,186].

4. Translational and Human Studies

4.1. Early Translational Studies

Early seminal studies in vibrational spectroscopy and radiation biology marked a significant step forward in the translational space [187–189], with investigations also including comparisons of dose-dependent spectral changes, utilisation of human tumour tissue, species comparison, and RS prediction of tumour response to EBRT in cervical cancers [190–192].

In the pursuit of advancing the clinical translation of vibrational spectroscopic techniques within the realm of radiation biology, numerous studies presented in the following sections articulate their findings through the use of medical terminology commonly employed by clinicians, such as sensitivity, specificity, accuracy, receiver operating characteristic (ROC) curves, and area under the curve (AUC). These classification metrics are critical in evaluating the diagnostic accuracy and predictive power of the spectroscopic methods in question, thereby bridging the gap between laboratory research and clinical application [193–195].

4.2. Analysis of Radiation Response in Humans with Liquid Biopsy Components

Liquid biopsies, such as blood, are an attractive sample choice for analysis because of the ability to provide a real-time view of the biomolecular composition of an individual with minimally invasive sample collection. Studies utilising RS have explored the effects of low-dose γ- and photon beam irradiation (0, 0.05 and 0.5 Gy) on isolated lymphocytes and peripheral blood mononuclear cells (PBMCs), respectively, revealing substantial inter-individual variability in radiosensitivity [86] and prediction of PBMC DNA damage in both prostate cancer patients and healthy volunteers [82].

X-ray radiation (56 Gy total)-induced muscle injury has been identified through a SERS band at 532 cm^{-1} in human serum and urine samples [196]. This band has been tentatively assigned to myoglobin. Additionally, SERS has been used to monitor radiotherapeutic treatment response in patients with nasopharyngeal carcinoma (NPC) [87].

FTIR and RS have demonstrated potential to distinguish plasma and lymphocyte spectral signatures in prostate cancer patients with minimal (grade 0–1) or severe (grade 2+) late toxicity following dose escalation in IMRT up to 81 Gy [75,76]. PLS-DA models constructed using dried plasma FTIR spectra have achieved classification sensitivities and specificities > 80% [75].

Analysis of in vitro sham irradiated (0 Gy) lymphocytes from patients with different late-toxicity grades has shown significant variations in spectral intensity of Raman bands related to numerous biomolecules (Figure 7A,B) [76].
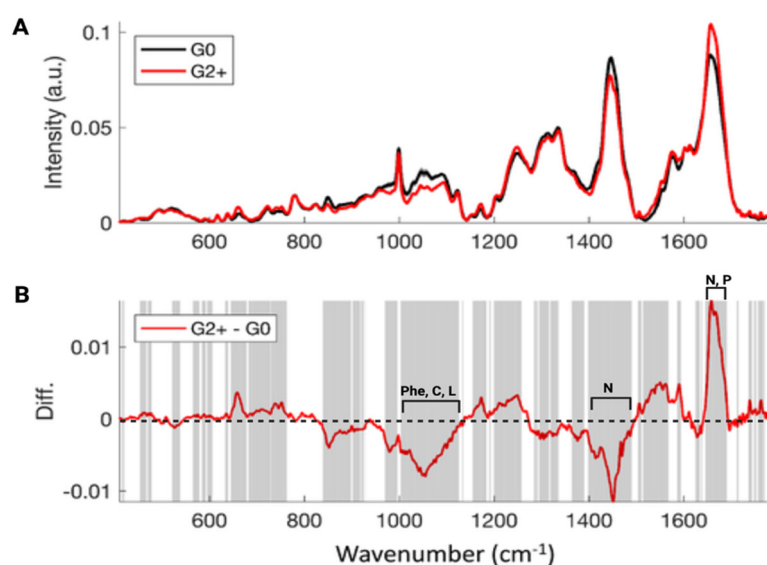

Figure 7. Mean and difference in Raman spectra of unirradiated lymphocytes from grade 0 to 1 (G0) and grade 2+ (G2+) high-risk prostate cancer patients; (**A**) The shaded region around each mean spectrum indicates the SE on the mean for each class. (**B**) Difference spectrum with grey shading represents regions of the spectrum that were found to be significantly different using a two-tailed *t*-test ($p < 0.05$). Phe = phenylalanine, C = carbohydrates, L = lipids, N = nucleic acids and P = proteins (amide I) [76].

Spectral differences in tandem with high PLS-DA classification rates achieved for lymphocytes (0 Gy) compared to those exposed to low photon doses suggest that intrinsic biochemical profiles can serve as reliable predictors of patient susceptibility to radiation toxicity, even in the absence of in vitro irradiation [76].

4.3. Analysis of Radiotherapeutic Treatment Response Using Tissue Biopsies

It has been demonstrated that RS and FTIR can predict treatment responses with high performance using pretreatment tissues from patients with rectal [88] and oesophageal [78] cancers and who received preoperative radiotherapy or neoadjuvant chemoradiotherapy (CRT), respectively. In particular, LDA of tissue (Figure 8A) from patients with rectal

cancer exhibiting a favourable response to radiotherapy (5 × 5 Gy) displayed positive scores (correlated with proteins and amino acids), while those with poor responses showed negative scores (linked to lipids; Figure 8B) [88].
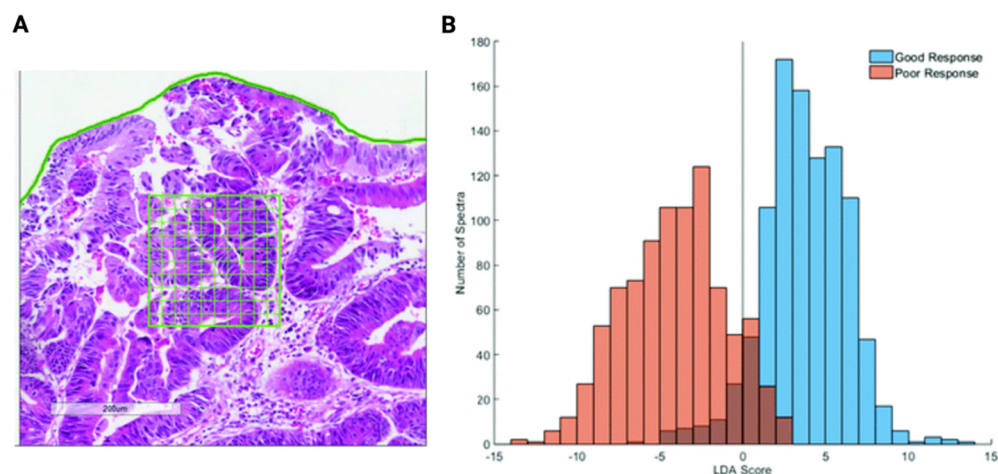

Figure 8. Raman and LDA analysis of a hematoxylin and eosin stained tissue biopsy from poor and good responding colorectal cancer patients to preoperative radiotherapy. (**A**) Example of a tissue section from colorectal cancer patients annotated for subsequent Raman analysis. (**B**) Histogram of the LDA scores [88].

In other work, prostate cancer patients treated with the first fraction of high-dose-rate brachytherapy (HDR-BT; 13.5 Gy) exhibited elevated glycogen and glucose (541, 847, 1123, and 1155 cm^{-1}) Raman spectral signatures [89], while decreased glycogen and cholesterol intensity ratios were observed in radioresistant glioblastoma neurospheres [197].

Furthermore, FTIR has provided insights into biomolecules associated with radiation-induced side effects experienced by patients with breast cancer, such as dermatitis [198].

A summary of investigations using tumour tissue and liquid biopsy components to demonstrate the predictive capabilities of vibrational spectroscopic methods in assessing the response to radiotherapy is presented in Table 1.

4.4. Analysis of Radiotherapeutic Treatment Response Using Bone Biopsies

Head and neck cancer (HNC) patients undergoing radiotherapy may experience alterations in the biochemical composition and quality of mandibular bone [199]. These modifications can adversely affect the outcomes of dental implants [200] and contribute to the pathogenesis of osteoradionecrosis (ORN) [201], a condition characterised by irreversible bone damage [202].

In investigating these effects, RS of bone samples from patients with oral squamous cell carcinoma who underwent radiotherapy and healthy controls did not show significant spectral differences [203]. However, compared to control bone, irradiated bone (<50 Gy or >50 Gy) from HNC patients revealed significant reductions ($p < 0.05$) in phosphate (960 cm^{-1}) and increases in carbonate modes (1070 cm^{-1}) [204] using RS, while FTIR analysis showed significant changes ($p < 0.05$) in the amide I region (1610–1710 cm^{-1}), but only in those receiving combined surgery, radiotherapy, and chemotherapy treatments [205].

Although the results here are promising, the translational application of vibrational spectroscopies in radiation science is in its infancy, the majority of studies being retrospective in nature, with limited sample size and a lack of validation cohorts. There is a need to transition to large-scale, multicentre prospective studies to showcase the potential clinical utility that vibrational spectroscopies hold.

Table 1. A summary of investigations using tumour tissue and liquid biopsy components to demonstrate the predictive capabilities of vibrational spectroscopic methods in assessing the response to radiotherapy.

Group	Sample Type	Population	Irradiation Mode	Observation Endpoint	Statistical and Prediction Methods
[86]	Isolated lymphocytes	Healthy donors ($n = 20$)	Low-dose γ-irradiation (0, 0.05 and 0.5 Gy)	At each dose, variation in classification performance was observed due to inter-individual intrinsic radiosensitivity. Sensitivities and specificities ranged from 65% to 100%.	PCA-LDA
[82]	Isolated PBMCs	Prostate cancer patients ($n = 22$) and healthy volunteers ($n = 26$)	Low-dose photon beam irradiation (0, 0.05 and 0.5 Gy)	Prediction of γ-H2AX fluorescence (DNA damage) from RS spectra (RMSEP = 1.59; uncertainty level of 5%)	SVM
[196]	Serum	Control ($n = 3$) and irradiated ($n = 45$) adult male BALB/C mice	X-ray (total body irradiation; 0, 2, 4, and Gy)	For all mice irradiated at doses 4 Gy and 6 Gy, the intensity of the myoglobin band (532 cm^{-1}) increased.	$p < 0.001$
[87]	Plasma	Pre-/post-RT NPC patients ($n = 40$) and healthy volunteers ($n = 30$)	NS	Classification sensitivities were 83.3% for differentiating pre-/post-RT samples, 61.8% for post-RT and healthy samples, and 95.1% for pre-RT and healthy samples, with specificities of 91.2%, 67.4%, and 93%, respectively.	PCA-LDA
[75]	Plasma	High-risk localised PCa patients with none or minimal late toxicity grade 0–1 ($n = 24$) and severe grade 2+ ($n = 11$)	IMRT Dose escalation up to 81 Gy	Classification sensitivity and specificity were 81.4% and 81.5%, respectively, for the differentiation of grade 0–1 and grade 2+ patients.	PLS-DA
[76]	Isolated lymphocytes	PCa patients with none or minimal late toxicity grade 0–1 ($n = 25$) and severe grade 2+ ($n = 17$)	IMRT Dose escalation up to 81 Gy. Following this, patient lymphocytes were in vitro photon irradiated (0, 0.05, and 0.5 Gy).	The classification performance of grade 0–1 and grade 2+ patients using unirradiated lymphocytes (0 Gy) were the highest, with sensitivity, specificity, and accuracy being 95%, 92%, and 93%, respectively.	PLS-DA
[88]	Pre-RT tumour biopsies	Rectal cancer patients who had a good ($n = 10$) and bad response ($n = 10$) following RT.	Preoperative 5 × 5 Gy short course RT	Classification of patient response to preoperative RT as good or poor obtained an accuracy of 86.04%	PCA-LDA
[78]	Pre-neo-CRT stromal and epithelial tissues	OC patients ($n = 50$)	Full course of neo-CRT	RS: Classification of patient epithelial and stromal tissue with TRG 1 to 4 returned AUC values of 82% and 85%, respectively. FTIR: Discrimination of OC patient tissue with TRG 1 to 5 was achieved with an AUC of 86%.	PCA-QDA and KNN were applied to RS and FTIR spectra, respectively.
[89]	Pre-/post-RT tissue biopsies	Intermediate risk PCa patients ($n = 9$)	Two fractions of HDR-BT (cumulative dose of 27 Gy)	Discrimination of pre-/post-RT tissues achieved accuracy, sensitivity, and specificity of 84.3%, 78.6% and 89.8%, respectively.	PCA-RF
[192]	Malignant cervix tissue biopsies	Responding (complete ($n = 18$) and partial ($n = 3$)) and non-responding ($n = 4$) patients	Two fractions of EBRT (cumulative dose of 4.5 Gy)	Using spectral region of 1250–1500 cm^{-1} patient spectra could be separated based on radiotherapeutic response.	Mahalanobis distance, and spectral residuals

NS = not specified, OC = oesophageal cancer, PCa = prostate cancer, RMSEP = root mean square error of prediction, RT = radiotherapy, TRG = tumour regression grade.

5. Discussion

Various types of ionising radiation (non-particulate (γ and X-rays) and particulate (α and protons)) [206] induce similar molecular oxidative stress [207–210] through the radiolysis of water, generating highly ROS such as superoxide anions ($O_2^{\bullet-}$), hydroxyl radical ($\bullet OH$), hydrated electrons ($e^-_{(aq)}$), and hydrogen peroxide (H_2O_2) [211]. ROS inflict significant molecular damage, leading to metabolic and functional modifications and initiation of various cell death processes [211,212]. Given that different modes of radiation induce similar biological effects at the molecular level, analysis using vibrational spectroscopy has elucidated consistent responses and trends, providing valuable insights into radiation-induced interactions and response mechanisms, as summarised here.

DNA damage and conformation changes: DNA damage resulting from oxidation is well established [213–215], including DNA base modifications and single- and double-strand breaks [216–218]. Spectroscopic investigations have identified nucleic base-unstacking spectral signatures [99,106,115,131,132] indicative of effects on base pairing and stacking. In addition, shifts to the mode, and modifications to the intensity of bands related to the vibration of the phosphodiester bonds and phosphate groups within the DNA backbone are suggestive of conformational changes to nucleic acids [107,108,110,113,114,121,138,141,142,171].

Lipid peroxidation: Phospholipid-dense cellular membranes are highly susceptible to radiation-induced lipid peroxidation, a process involving the removal of electrons by ROS [219]. Recent research has linked peroxidation of polyunsaturated fatty acids as a key driver of cellular membrane oxidation [220]. Lipid peroxidation processes lead to fatty acid chain breakdown and formation of degradation by-products, compromising membrane integrity and function [221], which in turn activates regulated cell death processes [220]. Spectroscopic evidence of lipid peroxidation includes variations in CH_2 and CH_3 stretching modes, as well as changes in cholesterol and its esters, olefinic=CH, and carbonyl groups [97,107,115,116,136,142,145,161,162,197].

Protein degradation and structural rearrangement: Similar to lipids, proteins are also key components of the cellular membrane, cytoplasm and nucleus [222]. Radiation has been reported to cause protein degradation (fragmentation, aggregation and oxidation) [223–225], as well as protein structural rearrangement [226]. ROS are mainly responsible for protein modifications [227], affecting overall protein structure and functionality [228–231]. Radiation-associated degradation and backbone conformational changes in protein biomolecules manifest spectroscopically as shifting and intensity modifications in secondary protein structures, particularly in the amide I, II, and III bands [76,95,98,102,105,107,116,121,133,136,163,183,184,205].

Metabolic influences: Gene and protein expression can be altered by radiation due to disturbances in functional metabolic mechanisms initiating a cascade of biological effects [232–235].

In particular, metabolic modulators of cellular glycogen metabolism (GSK-3β and AMP-activated kinase (AMPK)) have previously been implicated in biological responses to radiation using methods such as the clonogenic assay, MRI monitoring, immunoblotting/fluorescence [236–239]. However, the direct association between radiation-induced glycogen accumulation and radioresistance was first reported with RS [149], instigating further out-of-field investigations into the potential role of glycogen metabolism and radiotherapeutic responses [240]. Identification of spectroscopic markers associated with molecular mechanisms of metabolic dysregulation could potentially identify therapeutic targets for response manipulation with an aim to enhance the effectiveness of radiotherapy.

Importantly, several biological assays have validated the proof-of-concept FTIR and RS detection of radiation-induced biomolecular changes. For example, fluorescent sensors such as BODIPY C11 and LipidTOX™ have confirmed radiation-induced lipid peroxidation and changes in lipid droplet concentration in MCF7 [144] and PC3 [119] cells, respectively. In radioresistant NSCLC-H460 cells, radiation-induced glycogen accumulation was corroborated by Western blotting, which showed an increase in GSK-3β (glycogen synthase kinase-3 beta) signalling, highlighting a strong association between elevated glycogen levels and radioresistance [149]. Immunofluorescence imaging of NSCLC-H460 xenografts with

carbonic anhydrase IX (CAIX) further demonstrated that this radiogenic glycogen accumulation is linked to tissue hypoxia [153,166], as hypoxic tumours are known to overexpress CAIX [241]. Additionally, the categorisation of cells based on radiation response using spectral data was corroborated by the clonogenic assay [126,147], the 'gold standard' for assessing radiosensitivity [242]. Spectral signals indicative of radiation-induced DNA damage were also validated using the radiation response biomarker γ-H2AX [82,86] and the comet assay [84]. Validation of spectral observations with established assays underscores the reliability of RS and FTIR detection of the response to radiation.

Furthermore, compared with FTIR and RS, traditional radiobiological assays are limited in both specificity and sensitivity [243]. In terms of specificity, traditional techniques typically probe a single biological marker at a time, whereas FTIR and RS can detect multiple markers simultaneously. This multiplex capability makes these technologies more suitable for assessing radiotherapeutic responses, which involves a diverse array of biomolecules.

Both spectroscopies are highly sensitive methodologies capable of detecting radiation-induced biological responses across a range of doses, including low [112], clinical [84,148], high [81,119], and very high doses [106,181,184]. However, the sensitivity of various radiobiological assays can differ. For instance, metabolic activity assays like MTT (3-[4,5-dimethylthiazol-2-yl]-2,5-diphenyl tetrazolium bromide) assay, and DNA damage-based assays such as the γ-H2AX assay, exhibit high sensitivity at biologically relevant doses [244–248]. This sensitivity also extends to other DNA damage markers such as pATM (phosphorylated ataxia telangiectasia mutated) and 53BP1 (tumour suppressor P53 binding protein 1) [249,250]. In contrast, pulse-field gel electrophoresis (PFGE) is less accurate at detecting double-strand breaks at low doses, achieving higher sensitivity only at high doses [251,252].

Vibrational spectroscopic methods not only support and build upon previous findings regarding biological modifications induced by ionising radiation but also contribute to elucidating such changes. Additionally, these methods highlight that the biological response to radiation is influenced by factors such as intrinsic radiotherapeutic response, sample type, tissue origin, time of analysis post-irradiation, irradiation modality (direct or indirect), radiation type, dose, energy, and rate. It is worthy to note that the majority of studies included in this review involved low-linear energy transfer irradiation (X-ray and γ radiation) to investigate biomolecular responses.

6. Future Perspectives on the Applications of Vibrational Spectroscopy in Radiation Biology and Radiotherapeutic Practice

Vibrational spectroscopy is an emerging technology in biomedical research, offering unparalleled insights into biomolecular profiles and supporting advancements across myriad clinical applications [253–262]. In radiobiology and in radiotherapy, several key advancements will allow translation of the technology towards clinical applications.

In particular, the influence of pre-analytical clinical sampling and processing approaches on the spectroscopic signature for both liquid and solid biopsy material is now well known [263–267]. This will drive the development of standardised laboratory procedures to underpin reproducible and reliable spectroscopic analysis.

In the case of both FTIR and RS, tissue imaging often requires a substantial acquisition time. However, the development of quantum cascade [268,269] and fibre lasers [270], together with the emergence of both stimulated [271] and coherent anti-Stokes Raman spectroscopies [272,273], have significantly reduced imaging times.

Processing and analysing vibrational spectroscopic data also pose significant challenges, often requiring specialised expertise in computer programming languages. To democratise access, user-friendly automated data pre-processing, visualisation, and downstream analysis toolboxes have been developed (Figure 9A) [66,222–277].

Importantly, advances in miniaturising spectroscopic technology [278–284] and fibre-optic probes [285–290] have expanded the clinical applicability of these technologies, enabling their use in more versatile and patient-centric settings. Furthermore, Raman fibre-

optic probes have been successfully integrated with endoscopes [286] and puncture needle biopsy instrumentation (Figure 9B) [288]. These advancements showcase the potential of the technology towards live surgical decisions, routine procedures, and point-of-care early disease detection and prediction of therapeutic outcomes.

Underpinning these diagnostic and therapeutic applications are cloud-based data analytics, enabling simplified, swift, and efficient point-of-care diagnostics and prognostics, particularly in resource-limited settings as demonstrated by Heraud et al. [279] (Figure 9C). This innovative approach would prove particularly useful in the case of radiation bio-dosimetry for occupational or disaster-based exposure.

In addition, the integration of deep learning and other artificial intelligence (AI) techniques for data analysis will revolutionise spectroscopic applications within biomedical research in general and radiobiological applications in particular [291] through advanced, automated data modelling, providing on-the-fly diagnostics, prognostics, spectral identification, and model interpretation [292–305].
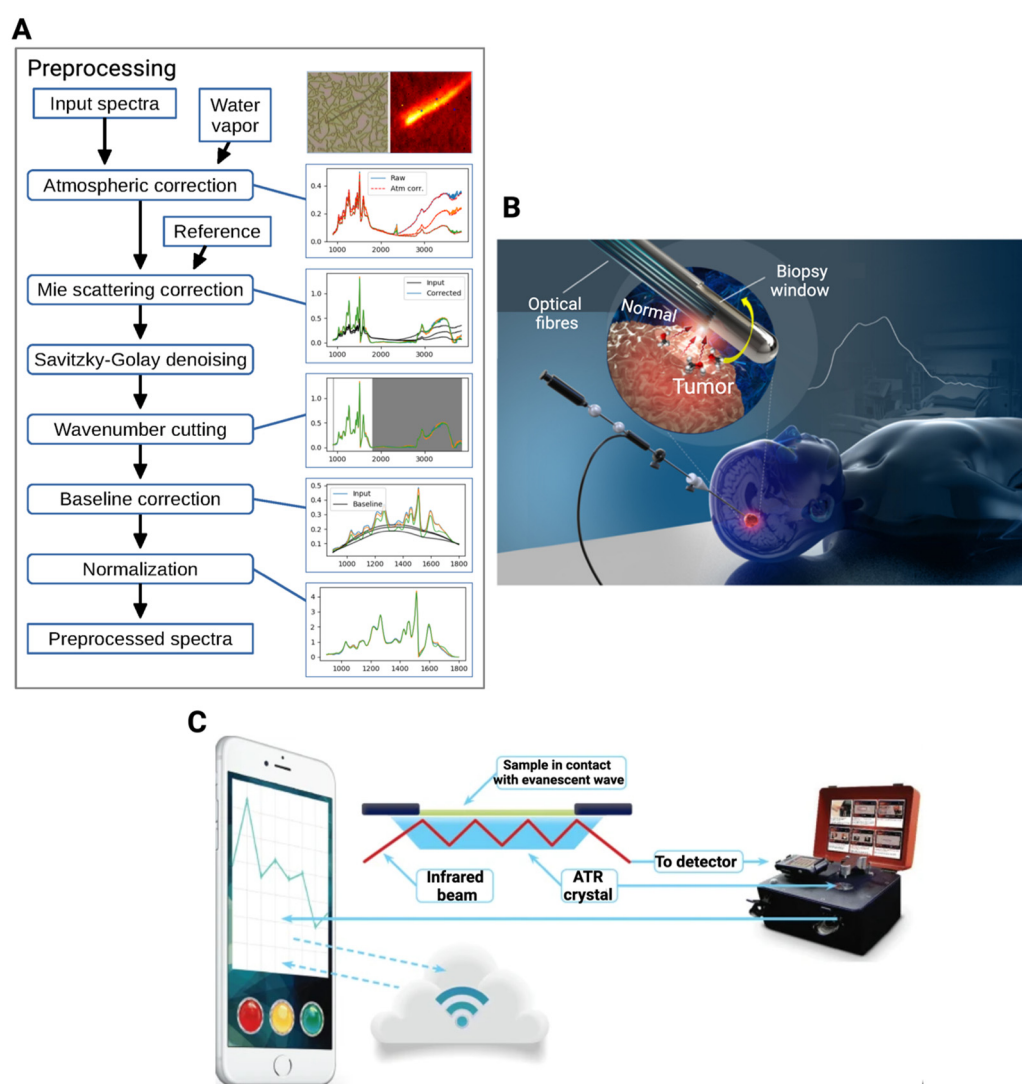

Figure 9. Examples of recent advancements in vibrational spectroscopy within biomedical and diagnostic contexts. (**A**) OCTAVSS graphical toolbox pre-processing flowchart for vibrational spectroscopy imaging data [66]. (**B**) Needle core biopsy integrated with a Raman spectrometer. Biopsy window magnified for clarity [288]. (**C**) Portable ATR–FTIR spectrometer integrated with cloud-based analytics for malaria diagnosis under tropical field conditions [279].

Spectroscopic technologies have strong potential for application in radiotherapeutic settings as an accurate, rapid, cost-effective, and minimally invasive assessment mode for individual responses to radiotherapy regimens, before or at the early stages of treatment. Further efforts are needed to overcome translation barriers, though continued research in this domain, in conjunction with advanced data analysis methods, has the potential to drive the development of prognostic, diagnostic, monitoring, and surveillance techniques in the context of radiation exposure.

References

1. Edison, T.A. Effect of X-rays upon the eye. *Nature* **1896**, *53*, 421.
2. Daniel, J. THE X-RAYS. *Science* **1896**, *3*, 562–563. [CrossRef] [PubMed]
3. Franken, N.A.P.; Rodermond, H.M.; Stap, J.; Haveman, J.; Van Bree, C. Clonogenic assay of cells in vitro. *Nat. Protoc.* **2006**, *1*, 2315–2319. [CrossRef] [PubMed]
4. Rothkamm, K.; Horn, S.; Scherthan, H.; Rößler, U.; De Amicis, A.; Barnard, S.; Kulka, U.; Lista, F.; Meineke, V.; Braselmann, H.; et al. Laboratory Intercomparison on the γ-H2AX Foci Assay. *Radiat. Res.* **2013**, *180*, 149–155. [CrossRef] [PubMed]
5. Viau, M.; Testard, I.; Shim, G.; Morat, L.; Normil, M.D.; Hempel, W.M.; Sabatier, L. Global quantification of γH2AX as a triage tool for the rapid estimation of received dose in the event of accidental radiation exposure. *Mutat. Res. Toxicol. Environ. Mutagen.* **2015**, *793*, 123–131. [CrossRef]
6. Jung, J.; Seol, H.S.; Chang, S. The Generation and Application of Patient-Derived Xenograft Model for Cancer Research. *Cancer Res. Treat.* **2018**, *50*, 1–10. [CrossRef]
7. Chen, M.; Zhao, H. Next-generation sequencing in liquid biopsy: Cancer screening and early detection. *Hum. Genom.* **2019**, *13*, 34. [CrossRef]
8. Meissner, G.W.; Grimm, J.B.; Johnston, R.M.; Sutcliffe, B.; Ng, J.; Jefferis, G.S.X.E.; Cachero, S.; Lavis, L.D.; Malkesman, O. Optimization of fluorophores for chemical tagging and immunohistochemistry of Drosophila neurons. *PLoS ONE* **2018**, *13*, e0200759. [CrossRef]
9. Gullo, R.L.; Daimiel, I.; Morris, E.A.; Pinker, K. Combining molecular and imaging metrics in cancer: Radiogenomics. *Insights Into Imaging* **2020**, *11*, 1. [CrossRef]
10. Rooprai, H.K.; Lawrence, P.; Keshavarz, S.; Yashod, P.; Gullan, R.W.; Selway, R.P.; Davies, D. DRAQ7 as an Alternative to MTT Assay for Measuring Viability of Glioma Cells Treated with Polyphenols. *Anticancer Res.* **2020**, *40*, 5427–5436. [CrossRef]
11. Sicca, F.; Martinuzzi, D.; Montomoli, E.; Huckriede, A. Comparison of influenza-specific neutralizing antibody titers determined using different assay readouts and hemagglutination inhibition titers: Good correlation but poor agreement. *Vaccine* **2020**, *38*, 2527–2541. [CrossRef] [PubMed]
12. Shui, L.; Ren, H.; Yang, X.; Li, J.; Chen, Z.; Yi, C.; Zhu, H.; Shui, P. The Era of Radiogenomics in Precision Medicine: An Emerging Approach to Support Diagnosis, Treatment Decisions, and Prognostication in Oncology. *Front. Oncol.* **2021**, *10*, 570465. [CrossRef] [PubMed]
13. Cooper, J.S.; Fu, K.; Marks, J.; Silverman, S. Late effects of radiation therapy in the head and neck region. *Int. J. Radiat. Oncol.* **1995**, *31*, 1141–1164. [CrossRef] [PubMed]
14. Magné, N.; Chargari, C.; MacDermed, D.; Conforti, R.; Védrine, L.; Spano, J.-P.; Khayat, D. Tomorrow's targeted therapies in breast cancer patients: What is the risk for increased radiation-induced cardiac toxicity? *Crit. Rev. Oncol.* **2010**, *76*, 186–195. [CrossRef]
15. Dreyfuss, A.D.; Velalopoulou, A.; Avgousti, H.; Bell, B.I.; Verginadis, I.I. Preclinical models of radiation-induced cardiac toxicity: Potential mechanisms and biomarkers. *Front. Oncol.* **2022**, *12*, 920867. [CrossRef]
16. Yu, Z.; Xu, C.; Song, B.; Zhang, S.; Chen, C.; Li, C.; Zhang, S. Tissue fibrosis induced by radiotherapy: Current understanding of the molecular mechanisms, diagnosis and therapeutic advances. *J. Transl. Med.* **2023**, *21*, 708. [CrossRef]
17. Nuryadi, E.; Mayang Permata, T.B.; Komatsu, S.; Oike, T.; & Nakano, T. Inter-assay precision of clonogenic assays for radiosensitivity in cancer cell line A549. *Oncotarget* **2018**, *9*, 13706–13712. [CrossRef]
18. Guogytė, K.; Plieskienė, A.; Ladygienė, R.; Sevriukova, O.; Janušonis, V.; Žiliukas, J. Assessment of Correlation between Chromosomal Radiosensitivity of Peripheral Blood Lymphocytes after In vitro Irradiation and Normal Tissue Side Effects for Cancer Patients Undergoing Radiotherapy. *Genome Integr.* **2017**, *8*, 2. [CrossRef]

19. Li, Z.; Li, N.; Shen, L.; Fu, J. Quantitative Proteomic Analysis Identifies MAPK15 as a Potential Regulator of Radioresistance in Nasopharyngeal Carcinoma Cells. *Front. Oncol.* **2018**, *8*, 548. [CrossRef]

20. Wang, T.-M.; Shen, G.-P.; Chen, M.-Y.; Zhang, J.-B.; Sun, Y.; He, J.; Xue, W.-Q.; Li, X.-Z.; Huang, S.-Y.; Zheng, X.-H.; et al. Genome-Wide Association Study of Susceptibility Loci for Radiation-Induced Brain Injury. *JNCI J. Natl. Cancer Inst.* **2018**, *111*, 620–628. [CrossRef]

21. Lobachevsky, P.N.; Bucknell, N.W.; Mason, J.; Russo, D.; Yin, X.; Selbie, L.; Ball, D.L.; Kron, T.; Hofman, M.; Siva, S.; et al. Monitoring DNA Damage and Repair in Peripheral Blood Mononuclear Cells of Lung Cancer Radiotherapy Patients. *Cancers* **2020**, *12*, 2517. [CrossRef] [PubMed]

22. Feynman, R.P. *QED: The Strange Theory of Light and Matter*; Princeton University Press: Princeton, NJ, USA, 1985.

23. Puppels, G.J.; de Mul, F.F.M.; Otto, C.; Greve, J.; Robert-Nicoud, M.; Arndt-Jovin, D.J.; Jovin, T.M. Studying single living cells and chromosomes by confocal Raman microspectroscopy. *Nature* **1990**, *347*, 301–303. [CrossRef] [PubMed]

24. Puppels, G.; Olminkhof, J.; Otto, C.; de Mul, F.; Greve, J. Laser irradiation and Raman spectroscopy of single living cells and chromosomes: Sample degradation occurs with 514.5 nm but not with 660 nm laser light. *Exp. Cell Res.* **1991**, *195*, 361–367. [CrossRef] [PubMed]

25. Puppels, G.; Garritsen, H.; Segers-Nolten, G.; de Mul, F.; Greve, J. Raman microspectroscopic approach to the study of human granulocytes. *Biophys. J.* **1991**, *60*, 1046–1056. [CrossRef]

26. Mohamed, H.T.; Untereiner, V.; Sockalingum, G.D.; Brézillon, S. Implementation of infrared and Raman modalities for glycosaminoglycan characterization in complex systems. *Glycoconj. J.* **2017**, *34*, 309–323. [CrossRef]

27. Kast, R.E.; Tucker, S.C.; Killian, K.; Trexler, M.; Honn, K.V.; Auner, G.W. Emerging technology: Applications of Raman spectroscopy for prostate cancer. *Cancer Metastasis Rev.* **2014**, *33*, 673–693. [CrossRef]

28. Barth, A. Infrared spectroscopy of proteins. *Biochim. Biophys. Acta Bioenerg.* **2007**, *1767*, 1073–1101. [CrossRef]

29. Hynes, A.; A Scott, D.; Man, A.; Singer, D.L.; Sowa, M.G.; Liu, K.-Z. Molecular mapping of periodontal tissues using infrared microspectroscopy. *BMC Med. Imaging* **2005**, *5*, 2. [CrossRef]

30. Balan, V.; Mihai, C.-T.; Cojocaru, F.-D.; Uritu, C.-M.; Dodi, G.; Botezat, D.; Gardikiotis, I. Vibrational spectroscopy fingerprinting in medicine: From molecular to clinical practice. *Materials* **2019**, *12*, 2884. [CrossRef]

31. Sato, S.; Sekine, R.; Kagoshima, H.; Kazama, K.; Kato, A.; Shiozawa, M.; Tanaka, J.-I. All-in-one Raman spectroscopy approach to diagnosis of colorectal cancer: Analysis of spectra in the fingerprint regions. *J. Anus Rectum Colon* **2019**, *3*, 84–90. [CrossRef]

32. Movasaghi, Z.; Rehman, S.; Rehman, I.U. Raman Spectroscopy of Biological Tissues. *Appl. Spectrosc. Rev.* **2007**, *42*, 493–541. [CrossRef]

33. Movasaghi, Z.; Rehman, S.; Rehman, I.U. Fourier Transform Infrared (FTIR) Spectroscopy of Biological Tissues. *Appl. Spectrosc. Rev.* **2008**, *43*, 134–179. [CrossRef]

34. Talari, A.C.S.; Movasaghi, Z.; Rehman, S.; Rehman, I.U. Raman Spectroscopy of Biological Tissues. *Appl. Spectrosc. Rev.* **2015**, *50*, 46–111. [CrossRef]

35. Cooper, J.B.; Marshall, S.; Jones, R.; Abdelkader, M.; Wise, K.L. Spatially compressed dual-wavelength excitation Raman spectrometer. *Appl. Opt.* **2014**, *53*, 3333–3340. [CrossRef]

36. Lunter, D.; Klang, V.; Kocsis, D.; Varga-Medveczky, Z.; Berkó, S.; Erdő, F. Novel aspects of Raman spectroscopy in skin research. *Exp. Dermatol.* **2022**, *31*, 1311–1329. [CrossRef]

37. Kerr, L.T.; Byrne, H.J.; Hennelly, B.M. Optimal choice of sample substrate and laser wavelength for Raman spectroscopic analysis of biological specimen. *Anal. Methods* **2015**, *7*, 5041–5052. [CrossRef]

38. Hepting, M. *Ordering Phenomena in Rare-Earth Nickelate Heterostructures*; Springer International Publishing AG: Cham, Switzerland, 2017.

39. Wang, J.; Jiang, Q.; Han, D. Multi-channel beam splitters based on gradient metasurfaces. *Results Phys.* **2021**, *24*, 104084. [CrossRef]

40. Enciso-Martinez, A.; Van Der Pol, E.; Hau, C.M.; Nieuwland, R.; Van Leeuwen, T.G.; Terstappen, L.W.; Otto, C. Label-free identification and chemical characterisation of single extracellular vesicles and lipoproteins by synchronous Rayleigh and Raman scattering. *J. Extracell. Vesicles* **2020**, *9*, 1730134. [CrossRef]

41. Jones, R.R.; Hooper, D.C.; Zhang, L.; Wolverson, D.; Valev, V.K. Raman techniques: Fundamentals and frontiers. *Nanoscale Res. Lett.* **2019**, *14*, 231. [CrossRef]

42. Yang, B.; Morris, M.D.; Owen, H. Holographic Notch Filter for Low-Wavenumber Stokes and Anti-Stokes Raman Spectroscopy. *Appl. Spectrosc.* **1991**, *45*, 1533–1536. [CrossRef]

43. Elliott, A.D. Confocal Microscopy: Principles and Modern Practices. *Curr. Protoc. Cytom.* **2020**, *92*, e68. [CrossRef] [PubMed]

44. Byrne, H.J.; Sockalingum, G.D.; Stone, N. Raman Microscopy: Complement or Competitor? In *Biomedical Applications of Synchrotron Infrared Microspectroscopy*; Williams, G., Fisher, S., Sule-Suso, J., Eds.; The Royal Society of Chemistry: London, UK, 2010; pp. 105–143. [CrossRef]

45. Luhmann, T.; Robson, S.; Kyle, S.; Boehm, J. *Close-Range Photogrammetry and 3D Imaging*; Walter de Gruyter GmbH: Berlin, Germany, 2019.

46. Giechaskiel, B.; Clairotte, M. Fourier Transform Infrared (FTIR) Spectroscopy for Measurements of Vehicle Exhaust Emissions: A Review. *Appl. Sci.* **2021**, *11*, 7416. [CrossRef]

47. Gazi, E.; Baker, M.; Dwyer, J.; Lockyer, N.P.; Gardner, P.; Shanks, J.H.; Reeve, R.S.; Hart, C.A.; Clarke, N.W.; Brown, M.D. A correlation of FTIR spectra derived from prostate cancer biopsies with gleason grade and tumour stage. *Eur. Urol.* **2006**, *50*, 750–761. [CrossRef] [PubMed]

48. ThermoFisher Scientific. *Advanced FTIR Spectroscopy Principles, Experiments and Applications*; ThermoFisher Scientific: Waltham, MA, USA, 2021.

49. Hughes, C.; Isaacson, J.; Perry, A.; Sun, R.F.; Turner, J. Creating Superposition: The Beam Splitter. In *Quantum Computing for the Quantum Curious*; Springer International Publishing: Cham, Switzerland, 2021; pp. 17–28. [CrossRef]

50. Duarte, F.J. Chapter 11—Spectrometry and Interferometry. In *Tunable Laser Optics*; Academic Press: San Diego, CA, USA, 2003; pp. 227–248. [CrossRef]

51. Velasco, A.V.; Cheben, P.; Florjańczyk, M. Chapter 3—Spatial Heterodyne Fourier-Transform Waveguide Spectrometers. In *Progress in Optics*; Elsevier: Oxford, UK, 2014; pp. 159–208. [CrossRef]

52. Newman, J. *Physics of the Life Sciences*; Springer Science & Business: Media, NY, USA, 2010.

53. Herres, W.; Gronholz, J. *Understanding FTIR Data Processing Part 1: Data Acquisition and Fourier Transformation 1*; Bojker Analytische Messtechnik GmbH: Karlsruhe, Germany, 2007.

54. Barton, B.; Thomson, J.; Diz, E.L.; Portela, R. Chemometrics for Raman Spectroscopy Harmonization. *Appl. Spectrosc.* **2022**, *76*, 1021–1041. [CrossRef] [PubMed]

55. Bassan, P.; Kohler, A.; Martens, H.; Lee, J.; Byrne, H.J.; Dumas, P.; Gazi, E.; Brown, M.; Clarke, N.; Gardner, P. Resonant Mie Scattering (RMieS) correction of infrared spectra from highly scattering biological samples. *Analyst* **2010**, *135*, 268–277. [CrossRef]

56. Gil, E.M.; Cheburkanov, V.; Yakovlev, V.V. Denoising Raman spectra using a single layer convolutional model trained on simulated data. *J. Raman Spectrosc.* **2023**, *54*, 814–822. [CrossRef]

57. Yue, X.; Wang, K.; Yan, H.; Park, J.G.; Liang, Z.; Zhang, C.; Wang, B.; Shi, J. Generalized Wavelet Shrinkage of Inline Raman Spectroscopy for Quality Monitoring of Continuous Manufacturing of Carbon Nanotube Buckypaper. *IEEE Trans. Autom. Sci. Eng.* **2016**, *14*, 196–207. [CrossRef]

58. Gautam, R.; Vanga, S.; Ariese, F.; Umapathy, S. Review of multidimensional data processing approaches for Raman and infrared spectroscopy. *EPJ Tech. Instrum.* **2015**, *2*, 8. [CrossRef]

59. Kerr, L.T.; Domijan, K.; Cullen, I.; Hennelly, B.M. Applications of Raman spectroscopy to the urinary bladder for cancer diagnostics. *Photon-Lasers Med.* **2014**, *3*, 193–224. [CrossRef]

60. Liu, D.; Hennelly, B.; O'Neill, L.; Byrne, H.J. Investigation of wavenumber calibration for Raman spectroscopy using a polymer standard. In *Optical Sensing and Detection V. Optical Sensing and Detection*; Berghmans, F., Mignani, A.G., Eds.; SPIE: Strasbourg, France, 2018.

61. Dörfer, T.; Bocklitz, T.; Tarcea, N.; Schmitt, M.; Popp, J. Checking and Improving Calibration of Raman Spectra using Chemometric Approaches. *Z. Phys. Chem.* **2011**, *225*, 753–764. [CrossRef]

62. Kerr, L.; Hennelly, B. A multivariate statistical investigation of background subtraction algorithms for Raman spectra of cytology samples recorded on glass slides. *Chemom. Intell. Lab. Syst.* **2016**, *158*, 61–68. [CrossRef]

63. Geng, L.; Ma, M.; Wang, X.; Yu, W.; Jia, S.; Wang, H. Comparison of Eight Techniques for Reconstructing Multi-Satellite Sensor Time-Series NDVI Data Sets in the Heihe River Basin, China. *Remote Sens.* **2014**, *6*, 2024–2049. [CrossRef]

64. Kim, S.; Lee, S.H.; Min, S.Y.; Byun, K.M.; Lee, S.Y. Dual-modal cancer detection based on optical pH sensing and Raman spectroscopy. *J. Biomed. Opt.* **2017**, *22*, 1–6. [CrossRef] [PubMed]

65. Bruun, S.W.; Kohler, A.; Adt, I.; Sockalingum, G.D.; Manfait, M.; Martens, H. Correcting Attenuated Total Reflection—Fourier Transform Infrared Spectra for Water Vapor and Carbon Dioxide. *Appl. Spectrosc.* **2006**, *60*, 1029–1039. [CrossRef] [PubMed]

66. Troein, C.; Siregar, S.; De Beeck, M.O.; Peterson, C.; Tunlid, A.; Persson, P. OCTAVVS: A Graphical Toolbox for High-Throughput Preprocessing and Analysis of Vibrational Spectroscopy Imaging Data. *Methods Protoc.* **2020**, *3*, 34. [CrossRef]

67. Bassan, P.; Byrne, H.J.; Lee, J.; Bonnier, F.; Clarke, C.; Dumas, P.; Gazi, E.; Brown, M.D.; Clarke, N.W.; Gardner, P. Reflection contributions to the dispersion artefact in FTIR spectra of single biological cells. *Analyst* **2009**, *134*, 1171–1175. [CrossRef]

68. Stommel, M.; Wills, C. *Clinical Research: Concepts and Principles for Advanced Practice Nurses*; Lippincott Williams & Wilkins: Philadelphia, PA, USA, 2004.

69. Delac, K.; Grgic, M.; Bartlett, M. *Recent Advances in Face Recognition*; InTech: Vienna, Austria, 2008.

70. Esbensen, K.H.; Guyot, D.; Westad, F.; Houmoller, L.P. Multivariate Data Analysis. In *Practice: An Introduction to Multivariate Data Analysis and Experimental Design*; Camo Software Inc.: Oslo, Norway, 2002.

71. Song, W.; Wang, H.; Maguire, P.; Nibouche, O. Nearest clusters based partial least squares discriminant analysis for the classification of spectral data. *Anal. Chim. Acta* **2018**, *1009*, 27–38. [CrossRef]

72. Aminu, M.; Ahmad, N.A. Locality preserving partial least squares discriminant analysis for face recognition. *J. King Saud Univ.-Comput. Inf. Sci.* **2022**, *34*, 153–164. [CrossRef]

73. Ruiz-Perez, D.; Guan, H.; Madhivanan, P.; Mathee, K.; Narasimhan, G. So you think you can PLS-DA? *BMC Bioinform.* **2020**, *21* (Suppl. S1), 2. [CrossRef]

74. Meksiarun, P.; Aoki, P.H.B.; Van Nest, S.J.; Sobral-Filho, R.G.; Lum, J.J.; Brolo, A.G.; Jirasek, A. Breast cancer subtype specific biochemical responses to radiation. *Analyst* **2018**, *143*, 3850–3858. [CrossRef]

75. Medipally, D.K.; Nguyen, T.N.Q.; Bryant, J.; Untereiner, V.; Sockalingum, G.D.; Cullen, D.; Noone, E.; Bradshaw, S.; Finn, M.; Dunne, M.; et al. Monitoring radiotherapeutic response in prostate cancer patients using high throughput ftir spectroscopy of liquid biopsies. *Cancers* **2019**, *11*, 925. [CrossRef] [PubMed]

76. Cullen, D.; Bryant, J.; Maguire, A.; Medipally, D.; McClean, B.; Shields, L.; Noone, E.; Bradshaw, S.; Finn, M.; Dunne, M.; et al. Raman spectroscopy of lymphocytes for the identification of prostate cancer patients with late radiation toxicity following radiotherapy. *Transl. Biophotonics* **2020**, *2*, e201900035. [CrossRef]

77. Surmacki, J.M. Monitoring the effect of therapeutic doses of gamma irradiation on medulloblastoma by Raman spectroscopy. *Anal. Methods* **2020**, *12*, 383–391. [CrossRef]

78. Nguyen, T.N.Q.; Maguire, A.; Mooney, C.; Jackson, N.; Lynam-Lennon, N.; Weldon, V.; Muldoon, C.; Maguire, A.A.; O'Toole, D.; Ravi, N.; et al. Prediction of pathological response to neo-adjuvant chemoradiotherapy for oesophageal cancer using vibrational spectroscopy. *Transl. Biophotonics* **2021**, *3*, e202000014. [CrossRef]

79. Ciobanu, C.; Mcnairn, C.; Nyiri, B.; Chauhan, V.; Subedi, S.; Murugkar, S. Exploring the use of Raman Spectroscopy and Covariate-Adjusted Multivariate Analysis for the Detection of Irradiated Blood. *Radiat. Res.* **2023**, *199*, 396–405. [CrossRef]

80. Lasalvia, M.; Capozzi, V.; Perna, G. A Comparison of PCA-LDA and PLS-DA Techniques for Classification of Vibrational Spectra. *Appl. Sci.* **2022**, *12*, 5345. [CrossRef]

81. Roman, M.; Wrobel, T.P.; Panek, A.; Efeoglu, E.; Wiltowska-Zuber, J.; Paluszkiewicz, C.; Byrne, H.J.; Kwiatek, W.M. Exploring subcellular responses of prostate cancer cells to X-ray exposure by Raman mapping. *Sci. Rep.* **2019**, *9*, 8715. [CrossRef]

82. Meade, A.D.; Maguire, A.; Bryant, J.; Cullen, D.; Medipally, D.; White, L.; McClean, B.; Shields, L.; Armstrong, J.; Dunne, M.; et al. Prediction of DNA damage and G2 chromosomal radio-sensitivity ex vivo in peripheral blood mononuclear cells with label-free Raman micro-spectroscopy. *Int. J. Radiat. Biol.* **2019**, *95*, 44–53. [CrossRef]

83. Roman, M.; Wrobel, T.P.; Panek, A.; Paluszkiewicz, C.; Kwiatek, W.M. Physicochemical damage and early-stage biological response to X-ray radiation studied in prostate cancer cells by Raman spectroscopy. *J. Biophotonics* **2020**, *13*, e202000252. [CrossRef]

84. Roman, M.; Wrobel, T.P.; Panek, A.; Paluszkiewicz, C.; Kwiatek, W.M. Exploring subcellular responses of prostate cancer cells to clinical doses of X-rays by Raman microspectroscopy. *Spectrochim. Acta Part A Mol. Biomol. Spectrosc.* **2021**, *255*, 119653. [CrossRef]

85. Brereton, R.G.; Lloyd, G.R. Partial least squares discriminant analysis: Taking the magic away. *J. Chemom.* **2014**, *28*, 213–225. [CrossRef]

86. Maguire, A.; Vegacarrascal, I.; White, L.; McClean, B.; Howe, O.; Lyng, F.M.; Meade, A.D. Analyses of Ionizing Radiation Effects *In Vitro* in Peripheral Blood Lymphocytes with Raman Spectroscopy. *Radiat. Res.* **2015**, *183*, 407–416. [CrossRef] [PubMed]

87. Wu, Q.; Qiu, S.; Yu, Y.; Chen, W.; Lin, H.; Lin, D.; Feng, S.; Chen, R. Assessment of the radiotherapy effect for nasopharyngeal cancer using plasma surface-enhanced Raman spectroscopy technology. *Biomed. Opt. Express* **2018**, *9*, 3413–3423. [CrossRef] [PubMed]

88. Kirkby, C.J.; de Pablo, J.G.; Tinkler-Hundal, E.; Wood, H.M.; Evans, S.D.; West, N.P. Developing a Raman spectroscopy-based tool to stratify patient response to pre-operative radiotherapy in rectal cancer. *Analyst* **2021**, *146*, 581–589. [CrossRef]

89. Milligan, K.; Van Nest, S.J.; Deng, X.; Ali-Adeeb, R.; Shreeves, P.; Punch, S.; Costie, N.; Pavey, N.; Crook, J.M.; Berman, D.M.; et al. Raman spectroscopy and supervised learning as a potential tool to identify high-dose-rate-brachytherapy induced biochemical profiles of prostate cancer. *J. Biophotonics* **2022**, *15*, e202200121. [CrossRef]

90. Paidi, S.K.; Diaz, P.M.; Dadgar, S.; Jenkins, S.V.; Quick, C.M.; Griffin, R.J.; Dings, R.P.; Rajaram, N.; Barman, I. Label-Free Raman Spectroscopy Reveals Signatures of Radiation Resistance in the Tumor Microenvironment. *Cancer Res.* **2019**, *79*, 2054–2064. [CrossRef]

91. Marcus, M.A.; Corelli, J.C. Infrared Spectroscopy of the Photo- and Radiobiology of DNA Bases and Their Derivatives. *Radiat. Res.* **1974**, *57*, 20–37. [CrossRef]

92. Verma, S.P. Low levels of irradiation modify lipid domains in model membranes: A laser raman study. *Radiat. Res.* **1986**, *107*, 183–193. [CrossRef]

93. Verma, S.P.; Rastogi, A. Role of Proteins in Protection against Radiation-Induced Damage in Membranes. *Radiat. Res.* **1990**, *122*, 130–136. [CrossRef]

94. Verma, S.P.; Sonwalkar, N. Structural Changes in Plasma Membranes Prepared from Irradiated Chinese Hamster V79 Cells as Revealed by Raman Spectroscopy. *Radiat. Res.* **1991**, *126*, 27–35. [CrossRef]

95. Verma, S.; Singhal, A.; Sonwalkar, N. Ionizing radiation target groups of band 3 inserted into egg lecithin liposomes as determined by raman spectroscopy. *Int. J. Radiat. Biol.* **1993**, *63*, 279–288. [CrossRef] [PubMed]

96. Sailer, K.; Viaggi, S.; Nüsse, M. Kinetics of radiation- and cytochrome c-induced modifications in liposomes analysed by FT–Raman spectroscopy. *Biochim. Biophys. Acta (BBA)-Biomembr.* **1997**, *1329*, 259–268. [CrossRef]

97. Kinder, C.Z.; Wessels, J.M.R. gamma-Irradiation and UV-C light-induced lipid peroxidation: A Fourier transform-infrared absorption spectroscopic study. *Int. J. Radiat. Biol.* **1997**, *71*, 561–571. [CrossRef] [PubMed]

98. Torreggiani, A.; Tamba, M.; Manco, I.; Faraone-Mennella, M.R.; Ferreri, C.; Chatgilialoglu, C. Radiation damage of lysozyme in a biomimetic model: Some insights by Raman spectroscopy. *J. Mol. Struct.* **2005**, *744–747*, 767–773. [CrossRef]

99. Sailer, K. Radiation-induced structural modifications in dsDNA analysed by FT-Raman spectroscopy. *Int. J. Radiat. Biol.* **1996**, *69*, 601–613. [CrossRef]

100. Synytsya, A.; Alexa, P.; de Boer, J.; Loewe, M.; Moosburger, M.; Würkner, M.; Volka, K. Raman spectroscopic study of calf thymus DNA: An effect of proton- and γ-irradiation. *J. Raman Spectrosc.* **2007**, *38*, 1406–1415. [CrossRef]

101. Synytsya, A.; Alexa, P.; de Boer, J.; Loewe, M.; Moosburger, M.; Würkner, M.; Volka, K. Raman spectroscopic study of serum albumins: An effect of proton- and γ-irradiation. *J. Raman Spectrosc.* **2007**, *38*, 1646–1655. [CrossRef]
102. Xue, J.; Du, G.; Wang, Y. Effect of MeV proton irradiation on bovine serum albumin molecule. *Nucl. Instrum. Methods Phys. Res. Sect. B Beam Interact. Mater. At.* **2006**, *245*, 318–321. [CrossRef]
103. Dovbeshko, G.I.; Gridina, N.Y.; Kruglova, E.B.; Pashchuk, O.P. FTIR spectroscopy studies of nucleic acid damage. *Talanta* **2000**, *53*, 233–246. [CrossRef]
104. McGeehan, J.E.; Carpentier, P.; Royant, A.; Bourgeois, D.; Ravelli, R.B.G. X-ray radiation-induced damage in DNA monitored by online Raman. *J. Synchrotron Radiat.* **2006**, *14*, 99–108. [CrossRef]
105. Torreggiani, A.; Tamba, M.; Manco, I.; Faraone-Mennella, M.R.; Ferreri, C.; Chatgilialoglu, C. Investigation of radical-based damage of RNase A in aqueous solution and lipid vesicles. *Biopolymers* **2005**, *81*, 39–50. [CrossRef] [PubMed]
106. Shaw, C.P.; Jirasek, A. The Use of Ultraviolet Resonance Raman Spectroscopy in the Analysis of Ionizing-Radiation-Induced Damage in DNA. *Appl. Spectrosc.* **2009**, *63*, 412–422. [CrossRef] [PubMed]
107. Melin, A.-M.; Perromat, A.; Déléris, G. Sensitivity of Deinococcus radiodurans to γ-Irradiation: A novel approach by fourier transform infrared spectroscopy. *Arch. Biochem. Biophys.* **2001**, *394*, 265–274. [CrossRef] [PubMed]
108. Melin, A.-M.; Perromat, A.; Lorin, C.; Déléris, G. γ Irradiation and cellular damage in Kocuria rosea: Investigation by one- and two-dimensional infrared spectroscopy. *Arch. Biochem. Biophys.* **2002**, *408*, 211–219. [CrossRef]
109. Perromat, A.; Melin, A.; Lorin, C.; Deleris, G. Fourier transform IR spectroscopic appraisal of radiation damage in *Micrococcus luteus*. *Biopolymers* **2003**, *72*, 207–216. [CrossRef]
110. Letien, C.; Lafortune, R.; Shareck, F.; Lacroix, M. DNA analysis of a radiotolerant bacterium Pantoea agglomerans by FT-IR spectroscopy. *Talanta* **2007**, *71*, 1969–1975. [CrossRef]
111. Little, M.P.; Cahoon, E.K.; Kitahara, C.M.; Simon, S.L.; Hamada, N.; Linet, M.S. Occupational radiation exposure and excess additive risk of cataract incidence in a cohort of US radiologic technologists. *Occup. Environ. Med.* **2020**, *77*, 1–8. [CrossRef]
112. Allen, C.H.; Kumar, A.; Qutob, S.; Nyiri, B.J.; Chauhan, V.; Murugkar, S. Raman micro-spectroscopy analysis of human lens epithelial cells exposed to a low-dose-range of ionizing radiation. *Phys. Med. Biol.* **2017**, *63*, 025002. [CrossRef]
113. Lasalvia, M.; Perna, G.; Pisciotta, P.; Cammarata, F.P.; Manti, L.; Capozzi, V. Raman spectroscopy for the evaluation of the radiobiological sensitivity of normal human breast cells at different time points after irradiation by a clinical proton beam. *Analyst* **2019**, *144*, 2097–2108. [CrossRef]
114. Lasalvia, M.; Perna, G.; Manti, L.; Rasero, J.; Stramaglia, S.; Capozzi, V. Raman spectroscopy monitoring of MCF10A cells irradiated by protons at clinical doses. *Int. J. Radiat. Biol.* **2019**, *95*, 207–214. [CrossRef]
115. Lipiec, E.; Wood, B.R.; Kulik, A.; Kwiatek, W.M.; Dietler, G. Nanoscale Investigation into the Cellular Response of Glioblastoma Cells Exposed to Protons. *Anal. Chem.* **2018**, *90*, 7644–7650. [CrossRef] [PubMed]
116. Delfino, I.; Ricciardi, V.; Manti, L.; Lasalvia, M.; Lepore, M. Multivariate Analysis of Difference Raman Spectra of the Irradiated Nucleus and Cytoplasm Region of SH-SY5Y Human Neuroblastoma Cells. *Sensors* **2019**, *19*, 3971. [CrossRef] [PubMed]
117. Delfino, I.; Perna, G.; Ricciardi, V.; Lasalvia, M.; Manti, L.; Capozzi, V.; Lepore, M. X-ray irradiation effects on nuclear and membrane regions of single SH-SY5Y human neuroblastoma cells investigated by Raman micro-spectroscopy. *J. Pharm. Biomed. Anal.* **2019**, *164*, 557–573. [CrossRef] [PubMed]
118. Andolfi, L.; Meschini, R.; Filippi, S.; Bedolla, D.E.; Piccirilli, F.; Lepore, M.; Delfino, I. X-rays induced alterations in mechanical and biochemical properties of isolated SH-SY5Y nuclei. *Biochim. Biophys. Acta (BBA) Gen. Subj.* **2023**, *1867*, 130291. [CrossRef] [PubMed]
119. Roman, M.; Wrobel, T.P.; Panek, A.; Paluszkiewicz, C.; Kwiatek, W.M. Lipid droplets in prostate cancer cells and effect of irradiation studied by Raman microspectroscopy. *Biochim. Biophys. Acta (BBA) Mol. Cell Biol. Lipids* **2020**, *1865*, 158753. [CrossRef] [PubMed]
120. Yan, J.; Zhang, F.; Huang, Q. FTIR Microspectroscopy Probes Particle-Radiation Effect on HCT116 cells (p53$^{+/+}$, p53$^{-/-}$). *Radiat. Res.* **2018**, *189*, 156–164. [CrossRef]
121. Gault, N.; Lefaix, J.-L. Infrared microspectroscopic characteristics of radiation-induced apoptosis in human lymphocytes. *Radiat. Res.* **2003**, *160*, 238–250. [CrossRef]
122. Gault, N.; Rigaud, O.; Poncy, J.-L.; Lefaix, J.-L. Infrared microspectroscopy study of γ-irradiated and H_2O_2-treated human cells. *Int. J. Radiat. Biol.* **2005**, *81*, 767–779. [CrossRef]
123. Gault, N.; Rigaud, O.; Poncy, J.-L.; Lefaix, J.-L. Biochemical alterations in human cells irradiated with α particles delivered by macro- or microbeams. *Radiat. Res.* **2007**, *167*, 551–562. [CrossRef]
124. Meade, A.D.; Clarke, C.; Byrne, H.J.; Lyng, F.M. Fourier transform infrared microspectroscopy and multivariate methods for radiobiological dosimetry. *Radiat. Res.* **2010**, *173*, 225–237. [CrossRef]
125. Jafarzadeh, N.; Mani-Varnosfaderani, A.; Gilany, K.; Eynali, S.; Ghaznavi, H.; Shakeri-Zadeh, A. The molecular cues for the biological effects of ionizing radiation dose and post-irradiation time on human breast cancer SKBR3 cell line: A Raman spectroscopy study. *J. Photochem. Photobiol. B Biol.* **2018**, *180*, 1–8. [CrossRef] [PubMed]
126. Pansare, K.; Singh, S.R.; Chakravarthy, V.; Gupta, N.; Hole, A.; Gera, P.; Sarin, R.; Krishna, C.M. Raman Spectroscopy: An Exploratory Study to Identify Post-Radiation Cell Survival. *Appl. Spectrosc.* **2020**, *74*, 553–562. [CrossRef] [PubMed]
127. Zheng, Z.; Su, J.; Bao, X.; Wang, H.; Bian, C.; Zhao, Q.; Jiang, X. Mechanisms and applications of radiation-induced oxidative stress in regulating cancer immunotherapy. *Front. Immunol.* **2023**, *14*, 1247268. [CrossRef] [PubMed]

128. Chen, W.; Hu, G.-H. Biomarkers for enhancing the radiosensitivity of nasopharyngeal carcinoma. *Cancer Biol. Med.* **2015**, *12*, 23–32. [CrossRef]

129. Tsao, S.W.; Tsang, C.M.; Lo, K.W. Epstein–Barr virus infection and nasopharyngeal carcinoma. *Philos. Trans. R. Soc. B Biol. Sci.* **2017**, *372*, 20160270. [CrossRef]

130. Al-Anazi, A.E.; Alanazi, B.S.; Alshanbari, H.M.; Masuadi, E.; Hamed, M.E.; Dandachi, I.; Alkathiri, A.; Hanif, A.; Nour, I.; Fatani, H.; et al. Increased Prevalence of EBV Infection in Nasopharyngeal Carcinoma Patients: A Six-Year Cross-Sectional Study. *Cancers* **2023**, *15*, 643. [CrossRef]

131. Qiu, S.; Weng, Y.; Li, Y.; Chen, Y.; Pan, Y.; Liu, J.; Lin, W.; Chen, X.; Li, M.; Lin, T.; et al. Raman profile alterations of irradiated human nasopharyngeal cancer cells detected with laser tweezer Raman spectroscopy. *RSC Adv.* **2020**, *10*, 14368–14373. [CrossRef]

132. Ou, L.; Chen, Y.; Su, Y.; Zou, C.; Chen, Z. Detection of Genomic DNA Damage from Radiated Nasopharyngeal Carcinoma Cells Using Surface-Enhanced Raman Spectroscopy (SERS). *Appl. Spectrosc.* **2016**, *70*, 1821–1830. [CrossRef]

133. Hill, I.E.; Boyd, M.; Milligan, K.; Jenkins, C.A.; Sorensen, A.; Jirasek, A.; Graham, D.; Faulds, K. Understanding radiation response and cell cycle variation in brain tumour cells using Raman spectroscopy. *Analyst* **2023**, *148*, 2594–2608. [CrossRef]

134. Rauniyar, S.; Pansare, K.; Sharda, A.; Singh, S.R.; Saha, P.; Chilakapati, M.K.; Gupta, S. Raman Spectroscopy Revealed Cell Passage-Dependent Distinct Biochemical Alterations in Radiation-Resistant Breast Cancer Cells. *ACS Omega* **2023**, *8*, 5522–5532. [CrossRef]

135. Xing, B.; Pu, C.; Chen, Y.; Sheng, Y.; Zhang, B.; Cui, J.; Wu, G.; Zhao, Y. Insights into the characteristics of primary radioresistant cervical cancer using single-cell transcriptomics. *Hum. Cell* **2023**, *36*, 1135–1146. [CrossRef] [PubMed]

136. Ricciardi, V.; Portaccio, M.; Manti, L.; Lepore, M. An FTIR Microspectroscopy Ratiometric Approach for Monitoring X-ray Irradiation Effects on SH-SY5Y Human Neuroblastoma Cells. *Appl. Sci.* **2020**, *10*, 2974. [CrossRef]

137. Qi, J.; Liu, B.; Li, Y.; Wu, D.; Tang, W. Raman spectroscopic study on Hela cells irradiated by X rays of different doses. *Chin. Opt. Lett.* **2009**, *7*, 734–737. [CrossRef]

138. Risi, R.; Manti, L.; Perna, G.; Lasalvia, M.; Capozzi, V.; Delfino, I.; Lepore, M. X-ray radiation-induced effects in human mammary epithelial cells investigated by Raman microspectroscopy. In *Progress in Biomedical Optics and Imaging—Proceedings of SPIE*; Society of Photo-Optical Instrumentation Engineers: Washington, DC, USA, 2012; p. 8427.

139. Delfino, I.; Camerlingo, C.; Capozzi, V.; Perna, G.; Manti, L.; Lepore, M. Interval-Principal Component Analysis of Raman spectra of single cells exposed to X-ray radiation. In Proceedings of the 2014 Fotonica AEIT Italian Conference on Photonics Technologies, Naples, Italy, 12–14 May 2014; p. 4. [CrossRef]

140. Delfino, I.; Perna, G.; Lasalvia, M.; Capozzi, V.; Manti, L.; Camerlingo, C.; Lepore, M. Visible micro-Raman spectroscopy of single human mammary epithelial cells exposed to x-ray radiation. *J. Biomed. Opt.* **2015**, *20*, 035003. [CrossRef]

141. Lipiec, E.; Birarda, G.; Kowalska, J.; Lekki, J.; Vaccari, L.; Wiecheć, A.; Wood, B.; Kwiatek, W. A new approach to studying the effects of ionising radiation on single cells using FTIR synchrotron microspectroscopy. *Radiat. Phys. Chem.* **2013**, *93*, 135–141. [CrossRef]

142. Lipiec, E.; Bambery, K.R.; Heraud, P.; Hirschmugl, C.; Lekki, J.; Kwiatek, W.M.; Tobin, M.J.; Vogel, C.; Whelan, D.; Wood, B.R. Synchrotron FTIR shows evidence of DNA damage and lipid accumulation in prostate adenocarcinoma PC-3 cells following proton irradiation. *J. Mol. Struct.* **2014**, *1073*, 134–141. [CrossRef]

143. Yousef, I.; Seksek, O.; Gil, S.; Prezado, Y.; Sulé-Suso, J.; Martínez-Rovira, I. Study of the biochemical effects induced by X-ray irradiations in combination with gadolinium nanoparticles in F98 glioma cells: First FTIR studies at the Emira laboratory of the SESAME synchrotron. *Analyst* **2016**, *141*, 2238–2249. [CrossRef]

144. Allen, C.H.; Skillings, R.; Ahmed, D.; Sanchez, S.C.; Altwasser, K.; Hilan, G.; Willmore, W.G.; Chauhan, V.; Cassol, E.; Murugkar, S. Investigating ionizing radiation-induced changes in breast cancer cells using stimulated Raman scattering microscopy. *J. Biomed. Opt.* **2023**, *28*, 076501. [CrossRef]

145. Simon, I.; Hedesiu, M.; Virag, P.; Salmon, B.; Tarmure, V.; Baciut, M.; Bran, S.; Jacobs, R.; Falamas, A. Raman Micro-Spectroscopy of Dental Pulp Stem Cells: An Approach to Monitor the Effects of Cone Beam Computed Tomography Low-Dose Ionizing Radiation. *Anal. Lett.* **2019**, *52*, 1097–1111. [CrossRef]

146. Matthews, Q.; Brolo, A.; Lum, J.; Duan, X.; Jirasek, A. Raman spectroscopy of single human tumour cells exposed to ionizing radiation *in vitro*. *Phys. Med. Biol.* **2011**, *56*, 19–38. [CrossRef]

147. Matthews, Q.; Jirasek, A.; Lum, J.J.; Brolo, A.G. Biochemical signatures of *in vitro* radiation response in human lung, breast and prostate tumour cells observed with Raman spectroscopy. *Phys. Med. Biol.* **2011**, *56*, 6839–6855. [CrossRef] [PubMed]

148. Harder, S.J.; Matthews, Q.; Isabelle, M.; Brolo, A.G.; Lum, J.J.; Jirasek, A. A Raman Spectroscopic Study of Cell Response to Clinical Doses of Ionizing Radiation. *Appl. Spectrosc.* **2015**, *69*, 193–204. [CrossRef] [PubMed]

149. Matthews, Q.; Isabelle, M.; Harder, S.J.; Smazynski, J.; Beckham, W.; Brolo, A.G.; Jirasek, A.; Lum, J.J. Radiation-Induced Glycogen Accumulation Detected by Single Cell Raman Spectroscopy Is Associated with Radioresistance that Can Be Reversed by Metformin. *PLoS ONE* **2015**, *10*, e0135356. [CrossRef] [PubMed]

150. Milligan, K.; Deng, X.; Shreeves, P.; Ali-Adeeb, R.; Matthews, Q.; Brolo, A.; Lum, J.J.; Andrews, J.L.; Jirasek, A. Raman spectroscopy and group and basis-restricted non negative matrix factorisation identifies radiation induced metabolic changes in human cancer cells. *Sci. Rep.* **2021**, *11*, 3853. [CrossRef]

151. Shreeves, P.; Andrews, J.L.; Deng, X.; Ali-Adeeb, R.; Jirasek, A. Nonnegative Matrix Factorization with Group and Basis Restrictions. *Stat. Biosci.* **2021**, *15*, 608–632. [CrossRef]

152. Deng, X.; Ali-Adeeb, R.; Andrews, J.L.; Shreeves, P.; Lum, J.J.; Brolo, A.; Jirasek, A. Monitor Ionizing Radiation-Induced Cellular Responses with Raman Spectroscopy, Non-Negative Matrix Factorization, and Non-Negative Least Squares. *Appl. Spectrosc.* **2020**, *74*, 701–711. [CrossRef]

153. Deng, X.; Milligan, K.; Brolo, A.; Lum, J.J.; Andrews, J.L.; Jirasek, A. Radiation treatment response and hypoxia biomarkers revealed by machine learning assisted Raman spectroscopy in tumour cells and xenograft tissues. *Analyst* **2022**, *147*, 5091–5104. [CrossRef]

154. Deng, X.; Milligan, K.; Ali-Adeeb, R.; Shreeves, P.; Brolo, A.; Lum, J.J.; Andrews, J.L.; Jirasek, A. Group and Basis Restricted Non-Negative Matrix Factorization and Random Forest for Molecular Histotype Classification and Raman Biomarker Monitoring in Breast Cancer. *Appl. Spectrosc.* **2022**, *76*, 462–474. [CrossRef]

155. Yasser, M.; Shaikh, R.; Chilakapati, M.K.; Teni, T. Raman spectroscopic study of radioresistant oral cancer sublines established by fractionated ionizing radiation. *PLoS ONE* **2014**, *9*, e97777. [CrossRef]

156. Bentzen, S.M.; Overgaard, J. Patient-to-patient variability in the expression of radiation-induced normal tissue injury. *Semin. Radiat. Oncol.* **1994**, *4*, 68–80. [CrossRef]

157. West, C.M.; Breat, Z. The independence of intrinsic radiosensitivity as a prognostic factor for patient response to radiotherapy of carcinoma of the cervix. *Br. J. Cancer* **1997**, *76*, 1184–1190. [CrossRef] [PubMed]

158. Amundson, S.A.; Do, K.T.; Vinikoor, L.C.; Lee, R.A.; Koch-Paiz, C.A.; Ahn, J.; Reimers, M.; Chen, Y.; Scudiero, D.A.; Weinstein, J.N.; et al. Integrating global gene expression and radiation survival parameters across the 60 cell lines of the national cancer institute anticancer drug screen. *Cancer Res.* **2008**, *68*, 415–424. [CrossRef] [PubMed]

159. Liberal, F.D.C.G.; McMahon, S.J. Characterization of Intrinsic Radiation Sensitivity in a Diverse Panel of Normal, Cancerous and CRISPR-Modified Cell Lines. *Int. J. Mol. Sci.* **2023**, *24*, 7861. [CrossRef] [PubMed]

160. Mollaee, P.F.; Azimian, H.; Ghadim, N.Z.; Dolat, E.; Sheykhoo, A.; Bahreyni-Toossi, M.-T. The role of intrinsic radiosensitivity in the low-dose adaptive response induction in human peripheral blood mononuclear cells. *J. Cancer Res. Ther.* **2023**, *19* (Suppl. S2), S737. [CrossRef] [PubMed]

161. Cakmak, G.; Zorlu, F.; Severcan, M.; Severcan, F. Screening of Protective Effect of Amifostine on Radiation-Induced Structural and Functional Variations in Rat Liver Microsomal Membranes by FT-IR Spectroscopy. *Anal. Chem.* **2011**, *83*, 2438–2444. [CrossRef]

162. Cakmak, G.; Miller, L.M.; Zorlu, F.; Severcan, F. Amifostine, a radioprotectant agent, protects rat brain tissue lipids against ionizing radiation induced damage: An FTIR microspectroscopic imaging study. *Arch. Biochem. Biophys.* **2012**, *520*, 67–73. [CrossRef]

163. Demir, P.; Akkas, S.B.; Severcan, M.; Zorlu, F.; Severcan, F. Ionizing Radiation Induces Structural and Functional Damage on the Molecules of Rat Brain Homogenate Membranes: A Fourier Transform Infrared (FT-IR) Spectroscopic Study. *Appl. Spectrosc.* **2015**, *69*, 154–164. [CrossRef]

164. Abdelrazzak, A.B.; El-Bahy, G.S. FT-IR spectroscopic investigation of ionizing radiation-induced damage in the small intestine of whole-body irradiated rats. *Vib. Spectrosc.* **2018**, *99*, 146–150. [CrossRef]

165. Harder, S.J.; Isabelle, M.; DeVorkin, L.; Smazynski, J.; Beckham, W.; Brolo, A.G.; Lum, J.J.; Jirasek, A. Raman spectroscopy identifies radiation response in human non-small cell lung cancer xenografts. *Sci. Rep.* **2016**, *6*, 21006. [CrossRef]

166. Van Nest, S.J.; Nicholson, L.M.; Pavey, N.; Hindi, M.N.; Brolo, A.G.; Jirasek, A.; Lum, J.J. Raman spectroscopy detects metabolic signatures of radiation response and hypoxic fluctuations in non-small cell lung cancer. *BMC Cancer* **2019**, *19*, 474. [CrossRef]

167. Vrbik, I.; Van Nest, S.J.; Meksiarun, P.; Loeppky, J.; Brolo, A.; Lum, J.J.; Jirasek, A. Haralick texture feature analysis for quantifying radiation response heterogeneity in murine models observed using Raman spectroscopic mapping. *PLoS ONE* **2019**, *14*, e0212225. [CrossRef] [PubMed]

168. Van Nest, S.J.; Nicholson, L.M.; DeVorkin, L.; Brolo, A.G.; Lum, J.J.; Jirasek, A. Raman Spectroscopic Signatures Reveal Distinct Biochemical and Temporal Changes in Irradiated Human Breast Adenocarcinoma Xenografts. *Radiat. Res.* **2018**, *189*, 497–504. [CrossRef] [PubMed]

169. Ali-Adeeb, R.N.; Shreeves, P.; Deng, X.; Milligan, K.; Brolo, A.G.; Lum, J.J.; Haston, C.; Andrews, J.L.; Jirasek, A. Raman microspectroscopy and machine learning for use in identifying radiation-induced lung toxicity. *PLoS ONE* **2022**, *17*, e0279739. [CrossRef] [PubMed]

170. Meade, A.D.; Howe, O.; Unterreiner, V.; Sockalingum, G.D.; Byrne, H.J.; Lyng, F.M. Vibrational spectroscopy in sensing radiobiological effects: Analyses of targeted and non-targeted effects in human keratinocytes. *Faraday Discuss.* **2013**, *187*, 213–234. [CrossRef]

171. Lipiec, E.; Bambery, K.R.; Lekki, J.M.; Tobin, J.; Vogel, C.; Whelan, D.R.; Wood, B.R. SR-FTIR Coupled with Principal Component Analysis Shows Evidence for the Cellular Bystander Effect. *Radiat. Res.* **2015**, *184*, 73–82. [CrossRef]

172. Slattery, C.; Nguyen, K.; Shields, L.; Vega-Carrascal, I.; Singleton, S.; Lyng, F.M.; McClean, B.; Meade, A.D. Application of Advanced Non-Linear Spectral Decomposition and Regression Methods for Spectroscopic Analysis of Targeted and Non-Targeted Irradiation Effects in an In-Vitro Model. *Int. J. Mol. Sci.* **2022**, *23*, 12986. [CrossRef]

173. Abdelrazzak, A.B.; Hezma, A.; El-Bahy, G.S. ATR-FTIR spectroscopy probing of structural alterations in the cellular membrane of abscopal liver cells. *Biochim. Biophys. Acta (BBA) Biomembr.* **2021**, *1863*, 183726. [CrossRef]

174. Camerlingo, C.; Verde, A.; Manti, L.; Meschini, R.; Delfino, I.; Lepore, M. Graphene-Based Raman Spectroscopy for pH Sensing of X-rays Exposed and Unexposed Culture Media and Cells. *Sensors* **2018**, *18*, 2242. [CrossRef]

175. Hübner, W.; Blume, A.; Pushnjakova, R.; Dekhtyar, Y.; Hein, H.-J. The Influence of X-ray Radiation on the Mineral/Organic Matrix Interaction of Bone Tissue: An FT-IR Microscopic Investigation. *Int. J. Artif. Organs* **2005**, *28*, 66–73. [CrossRef]

176. Green, D.E.; Adler, B.J.; Chan, M.E.; Lennon, J.J.; Acerbo, A.S.; Miller, L.M.; Rubin, C.T. Altered Composition of Bone as Triggered by Irradiation Facilitates the Rapid Erosion of the Matrix by Both Cellular and Physicochemical Processes. *PLoS ONE* **2013**, *8*, e64952. [CrossRef]

177. Gong, B.; Oest, M.E.; Mann, K.A.; Damron, T.A.; Morris, M.D. Raman spectroscopy Demonstrates Prolonged Alteration of Bone Chemical composition following extremity localized irradiation. *Bone* **2013**, *57*, 252–258. [CrossRef] [PubMed]

178. Tchanque-Fossuo, C.N.; Gong, B.; Poushanchi, B.; Donneys, A.; Sarhaddi, D.; Gallagher, K.K.; Deshpande, S.S.; Goldstein, S.A.; Morris, M.D.; Buchman, S.R. Raman spectroscopy demonstrates Amifostine induced preservation of bone mineralization patterns in the irradiated murine mandible. *Bone* **2013**, *52*, 712–717. [CrossRef] [PubMed]

179. Felice, P.A.; Gong, B.; Ahsan, S.; Deshpande, S.S.; Nelson, N.S.; Donneys, A.; Tchanque-Fossuo, C.; Morris, M.D.; Buchman, S.R. Raman spectroscopy delineates radiation-induced injury and partial rescue by amifostine in bone: A murine mandibular model. *J. Bone Miner. Metab.* **2015**, *33*, 279–284. [CrossRef]

180. Limirio, P.H.J.O.; Soares, P.B.F.; Emi, E.T.P.; Lopes, C.d.C.A.; Rocha, F.S.; Batista, J.D.; Rabelo, G.D.; Dechichi, P. Ionizing radiation and bone quality: Time-dependent effects. *Radiat. Oncol.* **2019**, *14*, 15. [CrossRef] [PubMed]

181. El-Hansi, N.S.; Said, H.H.; Desouky, O.S.; Khalaf, M.A.; Talaat, M.S.; Sallam, A.M. XRD and ATR-FTIR techniques for integrity assessment of gamma radiation sterilized cortical bone pretreated by antioxidants. *Cell Tissue Bank.* **2021**, *22*, 305–321. [CrossRef] [PubMed]

182. Kubisz, L.; Połomska, M. FT NIR Raman studies on γ-irradiated bone. *Spectrochim. Acta Part A Mol. Biomol. Spectrosc.* **2007**, *66*, 616–625. [CrossRef]

183. Barth, H.D.; Launey, M.E.; MacDowell, A.A.; Ager, J.W.; Ritchie, R.O. On the effect of X-ray irradiation on the deformation and fracture behavior of human cortical bone. *Bone* **2010**, *46*, 1475–1485. [CrossRef]

184. Barth, H.D.; Zimmermann, E.A.; Schaible, E.; Tang, S.Y.; Alliston, T.; Ritchie, R.O. Characterization of the effects of x-ray irradiation on the hierarchical structure and mechanical properties of human cortical bone. *Biomaterials* **2011**, *32*, 8892–8904. [CrossRef]

185. de Castro, P.A.A.; Dias, D.A.; Del-Valle, M.; Veloso, M.N.; Somessari, E.S.R.; Zezell, D.M. Assessment of bone dose response using ATR-FTIR spectroscopy: A potential method for biodosimetry. *Spectrochim. Acta Part A Mol. Biomol. Spectrosc.* **2022**, *273*, 120900. [CrossRef]

186. Lam, S.E.; Nawi, S.N.M.; Sani, S.F.A.; Khandaker, M.U.; Bradley, D.A. Raman and photoluminescence spectroscopy analysis of gamma irradiated human hair. *Sci. Rep.* **2021**, *11*, 7939. [CrossRef]

187. Jyothi Lakshmi, R.; Kartha, V.B.; Murali Krishna, C.; Solomon, J.G.R.; Ullas, G.; Uma Devi, P. Tissue Raman Spectroscopy for the Study of Radiation Damage: Brain Irradiation of Mice. *Radiat. Res.* **2002**, *157*, 175–182. [CrossRef] [PubMed]

188. Lakshmi, R.J.; Alexander, M.; Kurien, J.; Mahato, K.K.; Kartha, V.B. Osteoradionecrosis (ORN) of the Mandible: A Laser Raman Spectroscopic Study. *Appl. Spectrosc.* **2003**, *57*, 1100–1116. [CrossRef] [PubMed]

189. Toyran, N.; Zorlu, F.; Severcan, F. Effect of stereotactic radiosurgery on lipids and proteins of normal and hypoperfused rat brain homogenates: A Fourier transform infrared spectroscopy study. *Int. J. Radiat. Biol.* **2005**, *81*, 911–918. [CrossRef] [PubMed]

190. de Boer, J.; Synytsya, A.; Alexa, P.; Besserer, J.; Froschauer, S.; Loewe, M.; Moosburger, M.; Volka, K.; Würkner, M. The effect of proton-irradiation on the Raman spectroscopy of tissue samples. *Radiother. Oncol.* **2004**, *73*, S102–S104. [CrossRef]

191. Synytsya, A.; Alexa, P.; Besserer, J.; De Boer, J.; Froschauer, S.; Gerlach, R.; Loewe, M.; Moosburger, M.; Obstová, I.; Quicken, P.; et al. Raman spectroscopy of tissue samples irradiated by protons. *Int. J. Radiat. Biol.* **2004**, *80*, 581–591. [CrossRef]

192. Vidyasagar, M.S.; Maheedhar, K.; Vadhiraja, B.M.; Fernendes, D.J.; Kartha, V.B.; Krishna, C.M. Prediction of radiotherapy response in cervix cancer by Raman spectroscopy: A pilot study. *Biopolymers* **2008**, *89*, 530–537. [CrossRef]

193. Florkowski, C.M. Sensitivity, Specificity, Receiver-Operating Characteristic (ROC) Curves and Likelihood Ratios: Communicating the Performance of Diagnostic Tests. *Clin. Biochem. Rev.* **2008**, *29* (Suppl. S1), S83–S87.

194. Hajian-Tilaki, K. Receiver Operating Characteristic (ROC) Curve Analysis for Medical Diagnostic Test Evaluation. *Casp. J. Intern. Med.* **2013**, *4*, 627–635.

195. Carter, J.V.; Pan, J.; Rai, S.N.; Galandiuk, S. ROC-ing along: Evaluation and interpretation of receiver operating characteristic curves. *Surgery* **2016**, *159*, 1638–1645. [CrossRef]

196. Muhammad, M.; Shao, C.; Huang, Q. Label-free SERS diagnostics of radiation-induced injury via detecting the biomarker Raman signal in the serum and urine bio-samples based on Au-NPs array substrates. *Spectrochim. Acta Part A Mol. Biomol. Spectrosc.* **2019**, *223*, 117282. [CrossRef]

197. Kumar, S.; Visvanathan, A.; Arivazhagan, A.; Santhosh, V.; Somasundaram, K.; Umapathy, S. Assessment of Radiation Resistance and Therapeutic Targeting of Cancer Stem Cells: A Raman Spectroscopic Study of Glioblastoma. *Anal. Chem.* **2018**, *90*, 12067–12074. [CrossRef] [PubMed]

198. Markouizou, A.; Michali, E.; Mamareli, C.; Anastassopoulou, J.; Kolovou, P.; Mamarelis, I.; Theophanides, T. The Effect of Irradiation on the Skin upon Breast Cancer Radiotherapy Studied by FTIR Spectroscopy. *OBM Geriatr.* **2022**, *6*, 1–15. [CrossRef]

199. Delanian, S.; Lefaix, J.-L. The radiation-induced fibroatrophic process: Therapeutic perspective via the antioxidant pathway. *Radiother. Oncol.* **2004**, *73*, 119–131. [CrossRef] [PubMed]

200. Chambrone, L.; Mandia, J.; Shibli, J.; Romito, G.; Abrahao, M. Dental Implants Installed in Irradiated Jaws. *J. Dent. Res.* **2013**, *92*, 119S–130S. [CrossRef]

201. Nadella, K.R.; Kodali, R.M.; Guttikonda, L.K.; Jonnalagadda, A. Osteoradionecrosis of the Jaws: Clinico-Therapeutic Management: A Literature Review and Update. *J. Maxillofac. Oral Surg.* **2015**, *14*, 891–901. [CrossRef]

202. Iqbal, Z.; Kyzas, P. Analysis of the critical dose of radiation therapy in the incidence of Osteoradionecrosis in head and neck cancer patients: A case series. *BDJ Open* **2020**, *6*, 1–6. [CrossRef]

203. Singh, S.; Parviainen, I.; Dekker, H.; Schulten, E.A.J.M.; Ten Bruggenkate, C.M. Raman Microspectroscopy Demonstrates Alterations in Human Mandibular Bone after Radiotherapy. *J. Anal. Bioanal. Tech.* **2015**, *6*, 276. [CrossRef]

204. Padala, S.R.; Saikia, D.; Mikkonen, J.J.W.; Uurasjärvi, E.; Dekker, H.; Schulten, E.A.J.M.; Bravenboer, N.; Koistinen, A.; Chauhan, A.; Singh, S.P.; et al. Irradiation Induced Biochemical Changes in Human Mandibular Bone: A Raman Spectroscopic Study. *Appl. Spectrosc.* **2022**, *76*, 1165–1173. [CrossRef]

205. Palander, A.; Dekker, H.; Hyvarinen, M.; Rieppo, L.; Lyijynen, I.; Schulten, E.A.J.M.; Bruggenkate, C.M.T.; Koistinen, A.; Kullaa, A.; Turunen, M.J. Long-term changes in mandibular bone microchemical quality after radiation therapy and underlying systemic malignancy: A pilot study. *J. Innov. Opt. Health Sci.* **2021**, *14*, 2150019. [CrossRef]

206. Institute of Medicine (US) Committee to Study the Feasibility of, and Need for, Epidemiologic Studies of Adverse Reproductive Outcomes in the Families of Atomic Veterans. Basic Principles of Radiation Biology. In *Adverse Reproductive Outcomes in Families of Atomic Veterans: The Feasibility of Epidemiologic Studies*; National Academies Press: Washington, DC, USA, 1995.

207. Narayanan, P.K.; Goodwin, E.H.; Lehnert, B.E. Alpha particles initiate biological production of superoxide anions and hydrogen peroxide in human cells. *Cancer Res.* **1997**, *57*, 3963–3971.

208. Mitteer, R.A.; Wang, Y.; Shah, J.; Gordon, S.; Fager, M.; Butter, P.-P.; Kim, H.J.; Guardiola-Salmeron, C.; Carabe-Fernandez, A.; Fan, Y. Proton beam radiation induces DNA damage and cell apoptosis in glioma stem cells through reactive oxygen species. *Sci. Rep.* **2015**, *5*, 13961. [CrossRef]

209. Chusreeaeom, K.; Khamsuk, O. Effects of gamma irradiation on lipid peroxidation, survival and growth of turmeric in vitro culture. *J. Phys. Conf. Ser.* **2019**, *1285*, 012003. [CrossRef]

210. Jia, S.; Ge, S.; Fan, X.; Leong, K.W.; Ruan, J. Promoting reactive oxygen species generation: A key strategy in nanosensitizer-mediated radiotherapy. *Nanomedicine* **2021**, *16*, 759–778. [CrossRef] [PubMed]

211. Obrador, E.; Montoro, A. Ionizing Radiation, Antioxidant Response and Oxidative Damage: Radiomodulators. *Antioxidants* **2023**, *12*, 1219. [CrossRef]

212. Ping, Z.; Peng, Y.; Lang, H.; Cai, X.; Zeng, Z.; Wu, X.; Zeng, H.; Shao, L. Oxidative stress in radiation-induced cardiotoxicity. *Oxidat. Med. Cell. Longev.* **2020**, *1*, 3579143. [CrossRef]

213. Halliwell, B. Why and how should we measure oxidative DNA damage in nutritional studies? How far have we come? *Am. J. Clin. Nutr.* **2000**, *72*, 1082–1087. [CrossRef]

214. Gedik, C.M.; Boyle, S.P.; Wood, S.G.; Vaughan, N.J.; Collins, A.R. Oxidative stress in humans: Validation of biomarkers of DNA damage. *Carcinogenesis* **2002**, *23*, 1441–1446. [CrossRef]

215. Cooke, M.S.; Evans, M.D.; Dizdaroglu, M.; Lunec, J. Oxidative DNA damage: Mechanisms, mutation, and disease. *FASEB J. Off. Publ. Fed. Am. Soc. Exp. Biol.* **2003**, *17*, 1195–1214. [CrossRef]

216. Salmon, T.B.; Evert, B.A.; Song, B.; Doetsch, P.W. Biological consequences of oxidative stress-induced DNA damage in Saccharomyces cerevisiae. *Nucleic Acids Res.* **2004**, *32*, 3712–3723. [CrossRef]

217. Maynard, S.; Schurman, S.H.; Harboe, C.; de Souza-Pinto, N.C.; Bohr, V.A. Base excision repair of oxidative DNA damage and association with cancer and aging. *Carcinogenesis* **2009**, *30*, 2–10. [CrossRef]

218. Juan, C.A.; de la Lastra, J.M.P.; Plou, F.J.; Pérez-Lebeña, E. The Chemistry of Reactive Oxygen Species (ROS) Revisited: Outlining Their Role in Biological Macromolecules (DNA, Lipids and Proteins) and Induced Pathologies. *Int. J. Mol. Sci.* **2021**, *22*, 4642. [CrossRef] [PubMed]

219. Kiang, J.G.; Fukumoto, R.; Gorbunov, N.V. Lipid Peroxidation After Ionizing Irradiation Leads to Apoptosis and Autophagy. In *Lipid Peroxidation*; IntechOpen: London, UK, 2012. [CrossRef]

220. Mortensen, M.S.; Ruiz, J.; Watts, J.L. Polyunsaturated Fatty Acids Drive Lipid Peroxidation during Ferroptosis. *Cells* **2023**, *12*, 804. [CrossRef] [PubMed]

221. Maia, G.A.S.; Renó, C.d.O.; Medina, J.M.; da Silveira, A.B.; Mignaco, J.A.; Atella, G.C.; Cortes, V.F.; Barbosa, L.A.; Santos, H.d.L. The effect of gamma radiation on the lipid profile of irradiated red blood cells. *Ann. Hematol.* **2014**, *93*, 753–760. [CrossRef] [PubMed]

222. Watson, H. Biological membranes. *Essays Biochem.* **2015**, *59*, 43–69. [CrossRef] [PubMed]

223. Le Maire, M.; Thauvette, L.; de Foresta, B.; Viel, A.; Beauregard, G.; Potier, M. Effects of ionizing radiations on proteins. Evidence of non-random fragmentations and a caution in the use of the method for determination of molecular mass. *Biochem. J.* **1990**, *267*, 431–439. [CrossRef]

224. Reisz, J.A.; Bansal, N.; Qian, J.; Zhao, W.; Furdui, C.M. Effects of Ionizing Radiation on Biological Molecules—Mechanisms of Damage and Emerging Methods of Detection. *Antioxid. Redox Signal.* **2014**, *21*, 260–292. [CrossRef]

225. Bansal, R.; Jha, S.K.; Jha, N.K. Size-based Degradation of Therapeutic Proteins—Mechanisms, Modelling and Control. *Biomol. Concepts* **2021**, *12*, 68–84. [CrossRef]

226. Amlan, C.; Abhijeet, D. Effect of Low Power mm wave Irradiation on sedimentation, coagulation and light absorbance of purified Bovine Serum Albumin. *Helix* **2012**, *3*, 165–168.

227. Lalande, M.; Schwob, L.; Vizcaino, V.; Chirot, F.; Dugourd, P.; Schlathölter, T.; Poully, J. Direct Radiation Effects on the Structure and Stability of Collagen and Other Proteins. *ChemBioChem* **2019**, *20*, 2972–2980. [CrossRef]

228. Gillard, N.; Goffinont, S.; Buré, C.; Davidkova, M.; Maurizot, J.-C.; Cadene, M.; Spotheim-Maurizot, M. Radiation-induced oxidative damage to the DNA-binding domain of the lactose repressor. *Biochem. J.* **2007**, *403*, 463–472. [CrossRef]

229. Afify, A.E.-M.M.R.; Rashed, M.M.; Mahmoud, E.A. Effect of Gamma Radiation on Protein Profile, Protein Fraction and Solubility's of Three Oil Seeds: Soybean, Peanut and Sesame. *Not. Bot. Horti Agrobot. Cluj-Napoca* **2011**, *39*, 90–98. [CrossRef]

230. Zhang, R.K.; Lyu, J.H.; Li, T. Effects of Radiation on Protein. *J. Nutr. Oncol.* **2020**, *5*, 116–122. [CrossRef]

231. Bahreinipour, M.; Zarei, H.; Dashtestani, F.; Rashidiani, J.; Eskandari, K.; Zarandi, S.A.M.; Ardestani, S.K.; Watabe, H. Radio-protective effect of nanoceria and magnetic flower-like iron oxide microparticles on gamma radiation-induced damage in BSA protein. *AIMS Biophys.* **2021**, *8*, 124–142. [CrossRef]

232. Ghosh, S.P.; Singh, R.; Chakraborty, K.; Kulkarni, S.; Uppal, A.; Luo, Y.; Kaur, P.; Pathak, R.; Kumar, K.S.; Hauer-Jensen, M.; et al. Metabolomic Changes in Gastrointestinal Tissues after Whole Body Radiation in a Murine Model. *Mol. Biosyst.* **2013**, *9*, 723–731. [CrossRef]

233. Liu, H.; Wang, Z.; Zhang, X.; Qiao, Y.; Wu, S.; Dong, F.; Chen, Y. Selection of candidate radiation biomarkers in the serum of rats exposed to gamma-rays byGC/TOFMS-based metabolomics. *Radiat. Prot. Dosim.* **2013**, *154*, 9–17. [CrossRef]

234. Laiakis, E.C.; Mak, T.D.; Anizan, S.; Amundson, S.A.; Barker, C.A.; Wolden, S.L.; Brenner, D.J.; Fornace, A.J. Development of a metabolomic radiation signature in urine from patients undergoing total body irradiation. *Radiat. Res.* **2014**, *181*, 350–361. [CrossRef]

235. Menon, S.S.; Uppal, M.; Randhawa, S.; Cheema, M.S.; Aghdam, N.; Usala, R.L.; Ghosh, S.P.; Cheema, A.K.; Dritschilo, A. Radiation Metabolomics: Current Status and Future Directions. *Front. Oncol.* **2016**, *6*, 20. [CrossRef]

236. Thotala, D.K.; E Hallahan, D.; Yazlovitskaya, E.M. Glycogen synthase kinase 3β inhibitors protect hippocampal neurons from radiation-induced apoptosis by regulating MDM2-p53 pathway. *Cell Death Differ.* **2012**, *19*, 387–396. [CrossRef]

237. Jiang, X.; Perez-Torres, C.J.; Thotala, D.; Engelbach, J.A.; Yuan, L.; Cates, J.; Gao, F.; Drzymala, R.E.; Rich, K.M.; Schmidt, R.E.; et al. A GSK-3β inhibitor protects against radiation necrosis in mouse brain. *Int. J. Radiat. Oncol. Biol. Phys.* **2014**, *89*, 714–721. [CrossRef]

238. Sanli, T.; Steinberg, G.R.; Singh, G.; Tsakiridis, T. AMP-activated protein kinase (AMPK) beyond metabolism: A novel genomic stress sensor participating in the DNA damage response pathway. *Cancer Biol. Ther.* **2014**, *15*, 156–169. [CrossRef]

239. Rae, C.; Mairs, R.J. AMPK activation by AICAR sensitizes prostate cancer cells to radiotherapy. *Oncotarget* **2019**, *10*, 749–759. [CrossRef] [PubMed]

240. Zois, C.E.; Hendriks, A.M.; Haider, S.; Pires, E.; Bridges, E.; Kalamida, D.; Voukantsis, D.; Lagerholm, B.C.; Fehrmann, R.S.N.; Dunnen, W.F.A.D.; et al. Liver glycogen phosphorylase is upregulated in glioblastoma and provides a metabolic vulnerability to high dose radiation. *Cell Death Dis.* **2022**, *13*, 1–15. [CrossRef] [PubMed]

241. Ronca, R.; Supuran, C.T. Carbonic anhydrase IX: An atypical target for innovative therapies in cancer. *Biochim. Biophys. Acta (BBA) Rev. Cancer* **2024**, *1879*, 189120. [CrossRef] [PubMed]

242. Oike, T.; Komatsu, S.; Komatsu, Y.; Nachankar, A.; Darwis, N.D.M.; Shibata, A.; Ohno, T. Reporting of methodologies used for clonogenic assays to determine radiosensitivity. *J. Radiat. Res.* **2020**, *61*, 828–831. [CrossRef] [PubMed]

243. Tipatet, K.S.; Davison-Gates, L.; Tewes, T.J.; Fiagbedzi, E.K.; Elfick, A.; Neu, B.; Downes, A. Detection of acquired radioresistance in breast cancer cell lines using Raman spectroscopy and machine learning. *Analyst* **2021**, *146*, 3709–3716. [CrossRef]

244. Hong, S.; Kim, I.H. The Optimal Condition of Performing MTT Assay for the Determination of Radiation Sensitivity. *J. Korean Soc. Ther. Radiol. Oncol.* **2001**, *19*, 163–170.

245. Kjellström, J.; Kjellén, E.; Johnsson, A. In vitro radiosensitization by oxaliplatin and 5-fluorouracil in a human colon cancer cell line. *Acta Oncol.* **2005**, *44*, 687–693. [CrossRef]

246. Friesner, J.D.; Liu, B.; Culligan, K.; Britt, A.B. Ionizing radiation–dependent γ-H2AX focus formation requires ataxia telangiectasia mutated and ataxia telangiectasia mutated and Rad3-related. *Mol. Biol. Cell* **2005**, *16*, 2566–2576. [CrossRef]

247. Rothkamm, K.; Crosbie, J.C.; Daley, F.; Bourne, S.; Barber, P.R.; Vojnovic, B.; Cann, L.; Rogers, P.A.W. In situ biological dose mapping estimates the radiation burden delivered to 'spared' tissue between synchrotron x-ray microbeam radiotherapy tracks. *PLoS ONE* **2012**, *7*, e29853. [CrossRef]

248. Rai, Y.; Pathak, R.; Kumari, N.; Sah, D.K.; Pandey, S.; Kalra, N.; Soni, R.; Dwarakanath, B.S.; Bhatt, A.N. Mitochondrial biogenesis and metabolic hyperactivation limits the application of MTT assay in the estimation of radiation induced growth inhibition. *Sci. Rep.* **2018**, *8*, 1531. [CrossRef]

249. Georgescu, W.; Osseiran, A.; Rojec, M.; Liu, Y.; Bombrun, M.; Tang, J.; Costes, S.V. Characterizing the DNA Damage Response by Cell Tracking Algorithms and Cell Features Classification Using High-Content Time-Lapse Analysis. *PLoS ONE* **2015**, *10*, e0129438. [CrossRef] [PubMed]

250. Zhao, J.; Guo, Z.; Pei, S.; Song, L.; Wang, C.; Ma, J.; Jin, L.; Ma, Y.; He, R.; Zhong, J.; et al. pATM and γH2AX are effective radiation biomarkers in assessing the radiosensitivity of 12C6+ in human tumor cells. *Cancer Cell Int.* **2017**, *17*, 49. [CrossRef] [PubMed]

251. Lobrich, P.K.C.A.B.R.M. Non-random distribution of DNA double-strand breaks induced by particle irradiation. *Int. J. Radiat. Biol.* **1996**, *70*, 493–503. [CrossRef] [PubMed]

252. Barnard, S.; Bouffler, S.; Rothkamm, K. The shape of the radiation dose response for DNA double-strand break induction and repair. *Genome Integr.* **2013**, *4*, 1. [CrossRef]

253. Neugebauer, U.; Trenkmann, S.; Bocklitz, T.; Schmerler, D.; Kiehntopf, M.; Popp, J. Fast differentiation of SIRS and sepsis from blood plasma of ICU patients using Raman spectroscopy. *J. Biophotonics* **2014**, *7*, 232–240. [CrossRef]

254. Ho, C.-S.; Jean, N.; Hogan, C.A.; Blackmon, L.; Jeffrey, S.S.; Holodniy, M.; Banaei, N.; Saleh, A.A.E.; Ermon, S.; Dionne, J. Rapid identification of pathogenic bacteria using Raman spectroscopy and deep learning. *Nat. Commun.* **2019**, *10*, 4927. [CrossRef]

255. Huber, M.; Kepesidis, K.V.; Voronina, L.; Božić, M.; Trubetskov, M.; Harbeck, N.; Krausz, F.; Žigman, M. Stability of person-specific blood-based infrared molecular fingerprints opens up prospects for health monitoring. *Nat. Commun.* **2021**, *12*, 1511. [CrossRef]

256. Nogueira, M.S.; Leal, L.B.; Marcarini, W.D.; Pimentel, R.L.; Muller, M.; Vassallo, P.F.; Campos, L.C.G.; dos Santos, L.; Luiz, W.B.; Mill, J.G.; et al. Rapid diagnosis of COVID-19 using FT-IR ATR spectroscopy and machine learning. *Sci. Rep.* **2021**, *11*, 15409. [CrossRef]

257. Wang, L.; Liu, W.; Tang, J.-W.; Wang, J.-J.; Liu, Q.-H.; Wen, P.-B.; Wang, M.-M.; Pan, Y.-C.; Gu, B.; Zhang, X. Applications of Raman Spectroscopy in Bacterial Infections: Principles, Advantages, and Shortcomings. *Front. Microbiol.* **2021**, *12*, 683580. [CrossRef]

258. Hanna, K.; Krzoska, E.; Shaaban, A.M.; Muirhead, D.; Abu-Eid, R.; Speirs, V. Raman spectroscopy: Current applications in breast cancer diagnosis, challenges and future prospects. *Br. J. Cancer* **2022**, *126*, 1125–1139. [CrossRef]

259. Liu, K.; Zhao, Q.; Li, B.; Zhao, X. Raman Spectroscopy: A Novel Technology for Gastric Cancer Diagnosis. *Front. Bioeng. Biotechnol.* **2022**, *10*, 856591. [CrossRef] [PubMed]

260. Caixeta, D.C.; Lima, C.; Xu, Y.; Guevara-Vega, M.; Espindola, F.S.; Goodacre, R.; Zezell, D.M.; Sabino-Silva, R. Monitoring glucose levels in urine using FTIR spectroscopy combined with univariate and multivariate statistical methods. *Spectrochim. Acta Part A Mol. Biomol. Spectrosc.* **2023**, *290*, 122259. [CrossRef] [PubMed]

261. Lukose, J.; Barik, A.K.; George, S.D.; Murukeshan, V.M.; Chidangil, S. Raman spectroscopy for viral diagnostics. *Biophys. Rev.* **2023**, *15*, 199–221. [CrossRef] [PubMed]

262. Wu, X.; Shuai, W.; Chen, X.; Luo, C.; Chen, Y.; Shi, Y.; Li, Z.; Lv, X.; Chen, C.; Meng, X.; et al. Rapid screening for autoimmune diseases using Fourier transform infrared spectroscopy and deep learning algorithms. *Front. Immunol.* **2023**, *14*, 1328228. [CrossRef]

263. Lovergne, L.; Clemens, G.; Untereiner, V.; Lukaszweski, R.A.; Sockalingum, G.D.; Baker, M.J. Investigating optimum sample preparation for infrared spectroscopic serum diagnostics. *Anal. Methods* **2015**, *7*, 7140–7149. [CrossRef]

264. Lovergne, L.; Bouzy, P.; Untereiner, V.; Garnotel, R.; Baker, M.J.; Thiéfin, G.; Sockalingum, G.D. Biofluid infrared spectro-diagnostics: Pre-analytical considerations for clinical applications. *Faraday Discuss.* **2016**, *187*, 521–537. [CrossRef]

265. Lovergne, L.; Lovergne, J.; Bouzy, P.; Untereiner, V.; Offroy, M.; Garnotel, R.; Thiéfin, G.; Baker, M.J.; Sockalingum, G.D. Investigating pre-analytical requirements for serum and plasma based infrared spectro-diagnostic. *J. Biophotonics* **2019**, *12*, e201900177. [CrossRef]

266. Cameron, J.M.; Butler, H.J.; Anderson, D.J.; Christie, L.; Confield, L.; Spalding, K.E.; Finlayson, D.; Murray, S.; Panni, Z.; Rinaldi, C.; et al. Exploring pre-analytical factors for the optimisation of serum diagnostics: Progressing the clinical utility of ATR-FTIR spectroscopy. *Vib. Spectrosc.* **2020**, *109*, 103092. [CrossRef]

267. Monaghan, J.F.; Cullen, D.; Wynne, C.; Lyng, F.M.; Meade, A.D. Effect of pre-analytical variables on Raman and FTIR spectral content of lymphocytes. *Analyst* **2023**, *148*, 5422–5434. [CrossRef]

268. Hasenkampf, A.; Kröger, N.; Schönhals, A.; Petrich, W.; Pucci, A. Surface-enhanced mid-infrared spectroscopy using a quantum cascade laser. *Opt. Express* **2015**, *23*, 5670–5680. [CrossRef]

269. Kuepper, C.; Kallenbach-Thieltges, A.; Juette, H.; Tannapfel, A.; Großerueschkamp, F.; Gerwert, K. Quantum Cascade Laser-Based Infrared Microscopy for Label-Free and Automated Cancer Classification in Tissue Sections. *Sci. Rep.* **2018**, *8*, 7717. [CrossRef] [PubMed]

270. Chemometric Imaging STRALE (STimulated RAman LasEr), CRI-Chemometric Imaging. 2024. Available online: https://www.cambridgeramanimaging.com/coral/ (accessed on 25 April 2024).

271. Hu, F.; Shi, L.; Min, W. Biological imaging of chemical bonds by stimulated Raman scattering microscopy. *Nat. Methods* **2019**, *16*, 830–842. [CrossRef] [PubMed]

272. Cheng, J.-X.; Xie, X.S. Coherent Anti-Stokes Raman Scattering Microscopy: Instrumentation, Theory, and Applications. *J. Phys. Chem. B* **2004**, *108*, 827–840. [CrossRef]

273. Li, S.; Li, Y.; Yi, R.; Liu, L.; Qu, J. Coherent Anti-Stokes Raman Scattering Microscopy and Its Applications. *Front. Phys.* **2020**, *8*, 598420. [CrossRef]

274. Grant-Peters, M.; Rich-Griffin, C.; E Grant-Peters, J.; Cinque, G.; A Dendrou, C. Photizo: An open-source library for cross-sample analysis of FTIR spectroscopy data. *Bioinformatics* **2022**, *38*, 3490–3492. [CrossRef]

275. Liu, Y.-J.; Kyne, M.; Wang, S.; Wang, S.; Yu, X.-Y.; Wang, C. A User-Friendly Platform for Single-Cell Raman Spectroscopy Analysis. *Spectrochim. Acta Part A Mol. Biomol. Spectrosc.* **2022**, *282*, 121686. [CrossRef]

276. Schmidt, R.W.; Woutersen, S.; Ariese, F. RamanLIGHT—a graphical user-friendly tool for pre-processing and unmixing hyper-spectral Raman spectroscopy images. *J. Opt.* **2022**, *24*, 064011. [CrossRef]

277. Sheehy, G.; Picot, F.; Dallaire, F.; Ember, K.J.; Nguyen, T.; Petrecca, K.; Trudel, D.; Leblond, F. Open-sourced Raman spectroscopy data processing package implementing a baseline removal algorithm validated from multiple datasets acquired in human tissue and biofluids. *J. Biomed. Opt.* **2023**, *28*, 025002. [CrossRef]

278. Owens, N.A.; Laurentius, L.B.; Porter, M.D.; Li, Q.; Wang, S.; Chatterjee, D. Handheld Raman Spectrometer Instrumentation for Quantitative Tuberculosis Biomarker Detection: A Performance Assessment for Point-of-Need Infectious Disease Diagnostics. *Appl. Spectrosc.* **2018**, *72*, 1104–1115. [CrossRef]

279. Heraud, P.; Chatchawal, P.; Wongwattanakul, M.; Tippayawat, P.; Doerig, C.; Jearanaikoon, P.; Perez-Guaita, D.; Wood, B.R. Infrared spectroscopy coupled to cloud-based data management as a tool to diagnose malaria: A pilot study in a malaria-endemic country. *Malar. J.* **2019**, *18*, 348. [CrossRef]

280. Roy, S.; Perez-Guaita, D.; Bowden, S.; Heraud, P.; Wood, B.R. Spectroscopy goes viral: Diagnosis of hepatitis B and C virus infection from human sera using ATR-FTIR spectroscopy. *Clin. Spectrosc.* **2019**, *1*, 100001. [CrossRef]

281. Ali, A.; Nettey-Oppong, E.E.; Effah, E.; Yu, C.Y.; Muhammad, R.; Soomro, T.A.; Byun, K.M.; Choi, S.H. Miniaturized Raman Instruments for SERS-Based Point-of-Care Testing on Respiratory Viruses. *Biosensors* **2022**, *12*, 590. [CrossRef] [PubMed]

282. Soliman, C.; Tu, D.; Mabbott, S.; Coté, G.; Maitland, K. Portable, multi-modal Raman and fluorescence spectroscopic platform for point-of-care applications. *J. Biomed. Opt.* **2022**, *27*, 095006. [CrossRef] [PubMed]

283. Caixeta, D.C.; Carneiro, M.G.; Rodrigues, R.; Alves, D.C.T.; Goulart, L.R.; Cunha, T.M.; Espindola, F.S.; Vitorino, R.; Sabino-Silva, R. Salivary ATR-FTIR Spectroscopy Coupled with Support Vector Machine Classification for Screening of Type 2 Diabetes Mellitus. *Diagnostics* **2023**, *13*, 1396. [CrossRef]

284. Xiao, J.; Chen, Y.; Xu, T.; Zhang, X. Hand-held Raman spectrometer-based flexible plasmonic biosensor for label-free multiplex urinalysis. *Talanta* **2024**, *266*, 124966. [CrossRef]

285. Jermyn, M.; Mok, K.; Mercier, J.; Desroches, J.; Pichette, J.; Saint-Arnaud, K.; Bernstein, L.; Guiot, M.-C.; Petrecca, K.; Leblond, F. Intraoperative brain cancer detection with Raman spectroscopy in humans. *Sci. Transl. Med.* **2015**, *7*, 274ra19. [CrossRef]

286. Bergholt, M.S.; Lin, K.; Wang, J.; Zheng, W.; Xu, H.; Huang, Q.; Ren, L.; Ho, K.Y.; Srivastava, S.; Huang, Z.; et al. Simultaneous fingerprint and high-wavenumber fiber-optic Raman spectroscopy enhances real-timein vivodiagnosis of adenomatous polyps during colonoscopy. *J. Biophotonics* **2016**, *9*, 333–342. [CrossRef]

287. Stevens, O.; Petterson, I.E.I.; Day, J.C.C.; Stone, N. Developing fibre optic Raman probes for applications in clinical spectroscopy. *Chem. Soc. Rev.* **2016**, *45*, 1919–1934. [CrossRef]

288. Desroches, J.; Jermyn, M.; Pinto, M.; Picot, F.; Tremblay, M.-A.; Obaid, S.; Marple, E.; Urmey, K.; Trudel, D.; Soulez, G.; et al. A new method using Raman spectroscopy for in vivo targeted brain cancer tissue biopsy. *Sci. Rep.* **2018**, *8*, 1792. [CrossRef]

289. Kim, S.; Kim, W.; Bang, A.; Song, J.-Y.; Shin, J.-H.; Choi, S. Label-free breast cancer detection using fiber probe-based Raman spectrochemical biomarker-dominated profiles extracted from a mixture analysis algorithm. *Anal. Methods* **2021**, *13*, 3249–3255. [CrossRef]

290. Zhang, S.; Vasudevan, S.; Tan, S.P.H.; Olivo, M. Fiber optic probe-based ATR-FTIR spectroscopy for rapid breast cancer detection: A pilot study. *J. Biophotonics* **2023**, *16*, e202300199. [CrossRef]

291. Fuentes, A.M.; Narayan, A.; Milligan, K.; Lum, J.J.; Brolo, A.G.; Andrews, J.L.; Jirasek, A. Raman spectroscopy and convolutional neural networks for monitoring biochemical radiation response in breast tumour xenografts. *Sci. Rep.* **2023**, *13*, 1530. [CrossRef] [PubMed]

292. Lasch, P.; Stämmler, M.; Zhang, M.; Baranska, M.; Bosch, A.; Majzner, K. FT-IR Hyperspectral Imaging and Artificial Neural Network Analysis for Identification of Pathogenic Bacteria. *Anal. Chem.* **2018**, *90*, 8896–8904. [CrossRef] [PubMed]

293. Yan, H.; Yu, M.; Xia, J.; Zhu, L.; Zhang, T.; Zhu, Z. Tongue squamous cell carcinoma discrimination with Raman spectroscopy and convolutional neural networks. *Vib. Spectrosc.* **2019**, *103*, 102938. [CrossRef]

294. Shin, H.; Oh, S.; Hong, S.; Kang, M.; Kang, D.; Ji, Y.-G.; Choi, B.H.; Kang, K.-W.; Jeong, H.; Park, Y.; et al. Early-Stage Lung Cancer Diagnosis by Deep Learning-Based Spectroscopic Analysis of Circulating Exosomes. *ACS Nano* **2020**, *14*, 5435–5444. [CrossRef]

295. Chen, S.; Zhang, H.; Yang, X.; Shao, X.; Li, T.; Chen, N.; Chen, Z.; Xue, W.; Pan, J.; Liu, S. Raman Spectroscopy Reveals Abnormal Changes in the Urine Composition of Prostate Cancer: An Application of an Intelligent Diagnostic Model with a Deep Learning Algorithm. *Adv. Intell. Syst.* **2021**, *3*, 2000090. [CrossRef]

296. Guerrini, L.; Garcia-Rico, E.; O'loghlen, A.; Giannini, V.; Alvarez-Puebla, R.A. Surface-Enhanced Raman Scattering (SERS) Spectroscopy for Sensing and Characterization of Exosomes in Cancer Diagnosis. *Cancers* **2021**, *13*, 2179. [CrossRef]

297. Kothari, R.; Jones, V.; Mena, D.; Bermúdez Reyes, V.; Shon, Y.; Smith, J.P.; Schmolze, D.; Cha, P.D.; Lai, L.; Storrie-Lombardi, M.C.; et al. Raman spectroscopy and artificial intelligence to predict the Bayesian probability of breast cancer. *Sci. Rep.* **2021**, *11*, 6482. [CrossRef]

298. Azam, K.S.F.; Ryabchykov, O.; Bocklitz, T. A Review on Data Fusion of Multidimensional Medical and Biomedical Data. *Molecules* **2022**, *27*, 7448. [CrossRef]

299. Kanemura, Y.; Kanazawa, M.; Hashimoto, S.; Hayashi, Y.; Fujiwara, E.; Suzuki, A.; Ishii, T.; Goto, M.; Nozaki, H.; Inoue, T.; et al. Assessment of skin inflammation using near-infrared Raman spectroscopy combined with artificial intelligence analysis in an animal model. *Analyst* **2022**, *147*, 2843–2850. [CrossRef]

300. Liu, Z.; Su, W.; Ao, J.; Wang, M.; Jiang, Q.; He, J.; Gao, H.; Lei, S.; Nie, J.; Yan, X.; et al. Instant diagnosis of gastroscopic biopsy via deep-learned single-shot femtosecond stimulated Raman histology. *Nat. Commun.* **2022**, *13*, 4050. [CrossRef] [PubMed]

301. Ben Shlomo, I.; Frankenthal, H.; Laor, A.; Greenhut, A.K. Detection of SARS-CoV-2 infection by exhaled breath spectral analysis: Introducing a ready-to-use point-of-care mass screening method. *eClinicalMedicine* **2022**, *45*, 101308. [CrossRef] [PubMed]

302. Bellantuono, L.; Tommasi, R.; Pantaleo, E.; Verri, M.; Amoroso, N.; Crucitti, P.; Di Gioacchino, M.; Longo, F.; Monaco, A.; Naciu, A.M.; et al. An eXplainable Artificial Intelligence analysis of Raman spectra for thyroid cancer diagnosis. *Sci. Rep.* **2023**, *13*, 16590. [CrossRef] [PubMed]

303. Day, P.L.; Erdahl, S.; Rokke, D.L.; Wieczorek, M.; Johnson, P.W.; Jannetto, P.J.; Bornhorst, J.A.; Carter, R.E. Artificial Intelligence for Kidney Stone Spectra Analysis: Using Artificial Intelligence Algorithms for Quality Assurance in the Clinical Laboratory. *Mayo Clin. Proc. Digit. Health* **2023**, *1*, 1–12. [CrossRef]

304. Farooq, S.; Del-Valle, M.; dos Santos, M.O.; dos Santos, S.N.; Bernardes, E.S.; Zezell, D.M. Rapid identification of breast cancer subtypes using micro-FTIR and machine learning methods. *Appl. Opt.* **2023**, *62*, C80–C87. [CrossRef]

305. Contreras, J.; Mostafapour, S.; Popp, J.; Bocklitz, T. Siamese Networks for Clinically Relevant Bacteria Classification Based on Raman Spectroscopy. *Molecules* **2024**, *29*, 1061. [CrossRef]